

Article

A Human Ventricular Myocyte Model with a Refined Representation of Excitation-Contraction Coupling

Yukiko Himeno,¹ Keiichi Asakura,^{1,2} Chae Young Cha,^{1,3} Hiraku Memida,¹ Trevor Powell,⁴ Akira Amano,¹ and Akinori Noma^{1,*}

¹Biosimulation Research Center, College of Life Sciences, Ritsumeikan University, Shiga, Japan; ²Nippon Shinyaku Co., Ltd., Kyoto, Japan; ³Oxford Centre for Diabetes Endocrinology and Metabolism and ⁴Department of Pharmacology, University of Oxford, Oxford, UK

ABSTRACT Cardiac Ca^{2+} -induced Ca^{2+} release (CICR) occurs by a regenerative activation of ryanodine receptors (RyRs) within each Ca^{2+} -releasing unit, triggered by the activation of L-type Ca^{2+} channels (LCCs). CICR is then terminated, most probably by depletion of Ca^{2+} in the junctional sarcoplasmic reticulum (SR). Hinch et al. previously developed a tightly coupled LCC-RyR mathematical model, known as the Hinch model, that enables simulations to deal with a variety of functional states of whole-cell populations of a Ca^{2+} -releasing unit using a personal computer. In this study, we developed a membrane excitation-contraction model of the human ventricular myocyte, which we call the human ventricular cell (HuVEC) model. This model is a hybrid of the most recent HuVEC models and the Hinch model. We modified the Hinch model to reproduce the regenerative activation and termination of CICR. In particular, we removed the inactivated RyR state and separated the single step of RyR activation by LCCs into triggering and regenerative steps. More importantly, we included the experimental measurement of a transient rise in Ca^{2+} concentrations ($[\text{Ca}^{2+}]$, 10–15 μM) during CICR in the vicinity of Ca^{2+} -releasing sites, and thereby calculated the effects of the local Ca^{2+} gradient on CICR as well as membrane excitation. This HuVEC model successfully reconstructed both membrane excitation and key properties of CICR. The time course of CICR evoked by an action potential was accounted for by autonomous changes in an instantaneous equilibrium open probability of couplons. This autonomous time course was driven by a core feedback loop including the pivotal local $[\text{Ca}^{2+}]$, influenced by a time-dependent decay in the SR Ca^{2+} content during CICR.

INTRODUCTION

Our understanding of human cardiac cell physiology has been greatly facilitated by combining limited human experimental data with mathematical myocyte models based on detailed and systematic knowledge gained by conducting animal experiments (1–3). Two of the most recent models of human ventricular cells (HuVECs), the GPB model (4) and the ORd model (5), were based on an extensive review of human data for membrane excitation, and demonstrated ionic mechanisms underlying the action potential (AP) as well as the Ca^{2+} transients at various stimulus frequencies. However, what is still required is a cell model that incorporates the updated mechanisms of Ca^{2+} -induced Ca^{2+} release (CICR), since membrane excitation is largely modified by intracellular Ca^{2+} dynamics (6). Moreover, CICR is the key mechanism in coupling membrane excitation to muscle contraction.

The empirical equations used to describe CICR so far in most cardiac cell models are of limited use because they were largely simplified. For example, the functional coupling between L-type Ca^{2+} channels (LCCs) and ryanodine receptors (RyRs) was calculated by referring to

a time-dependent increase of $[\text{Ca}^{2+}]$ in a single dyadic (or submembrane) space common to the whole population of RyRs within a cell. However, it is now well established that CICR is regulated by the tight coupling between LCCs and a cluster of RyRs individually for each Ca^{2+} -releasing unit (CaRU) (7,8) (this is known as the local control theory). Here, we define the cluster of RyRs as a couplon separate from LCCs. Moreover, the activation and inactivation kinetics of RyR models have been elucidated in much more detail by recent experimental findings.

Greenstein and Winslow (9) formulated a computational model of the cardiac ventricular myocyte that included the stochastic calculation of 12,500 individual CaRUs gating according to the local control of CICR. Subsequently, Hinch (10) and Hinch et al. (11) succeeded in reducing the computational cost of that model by developing a new algorithm (a tightly coupled LCC-RyR model, known as the Hinch model) for calculating CICR processes explicitly for each combination of open or closed conformations of LCCs and a couplon, representing a hypothetical CaRU composed of a group of RyRs. In the Hinch model, the spread of activation to neighboring CaRUs is prevented by assuming that the released Ca^{2+} is largely diluted by the bulk cytosol separating individual CaRUs, and thus the activation of RyRs is roughly proportional to the LCC activation. However, it is well established that a large Ca^{2+} gradient

Submitted October 24, 2014, and accepted for publication June 11, 2015.

*Correspondence: noma@sk.ritsumeik.ac.jp

Editor: Andrew McCulloch.

© 2015 by the Biophysical Society
0006-3495/15/07/0415/13 \$2.00



occurs near the Ca^{2+} -releasing site (12–17). Any Ca^{2+} accumulation around a CaRU in general might allow the spread of sequential activation of neighbors through an increase in local $[\text{Ca}^{2+}]$ outside the CaRU.

A localized Ca^{2+} depletion within the SR has been observed during Ca^{2+} sparks by confocal imaging (18–20). The effects of this Ca^{2+} depletion were examined by theoretical calculations of the stochastic activation of individual RyRs induced by the spatiotemporal evolution of $[\text{Ca}^{2+}]$ within the dyadic cleft. It was demonstrated that the depletion of local Ca^{2+} content in the terminal cisternae of the sarcoplasmic reticulum (SR) did indeed terminate the Ca^{2+} release of CaRUs in the absence of an inactivation state of RyRs (SJ model (21), LC model (22), and SM model (23)).

The inactivation of LCC is also a pivotal element in calculating the time evolution of the state transitions of CaRUs. However, most models of Ca^{2+} -dependent inactivation (CDI) are not necessarily based on the cascade of molecular events of the CDI of LCCs (24–27). On the other hand, the Hinch model gives a Ca^{2+} concentration at the Ca^{2+} -binding site for CDI, which is consistent with the widely accepted theoretical estimation of $[\text{Ca}^{2+}]$ near the ion channel exit (25,26,28–30). If the estimation of $[\text{Ca}^{2+}]$ at the ion channel exit is realistic, the shortening of AP evoked by increasing the $[\text{Ca}^{2+}]_o$ (31,32) might be reproduced in a mathematical model through the CDI mechanism.

In our previous study (33), we used the Hinch model to examine the involvement of CICR in the development of early afterdepolarization (EAD) and delayed afterdepolarization (DAD) in a human ventricular myocyte model. Here, we decided that although the basic mechanisms of EAD and DAD would remain essentially the same, we had to improve the state transition of CaRU (11) by removing the rapid inactivation of RyR, since it has been reported that such inactivation is hardly observed in experiments (33–36). We revised the kinetics of the CICR model with respect to the Ca^{2+} dependency of the couplon closing rate, which was caused by the Ca^{2+} -dependent activation of individual RyRs that constitute the couplon. We incorporated this revised CICR model into our HuVEC model. Using this HuVEC model, we demonstrated mechanisms underlying both graded Ca^{2+} release in the presence of local Ca^{2+} accumulation, and the controlled termination of regenerative CICR in the absence of RyR inactivation. Although detailed experiments of CICR have not yet been conducted in HuVECs, it may be timely to propose a comprehensive human ventricular myocyte model that includes membrane mechanisms, mechanistic CICR models, and the contraction of myofilaments.

MATERIALS AND METHODS

Details regarding the parameters used in this work, the variables and their physical units, cell geometry, Ca^{2+} compartments, Ca^{2+} buffers, Ca^{2+} diffusion, dynamic equations for ion channels and transporters,

the CaRU, and changes in ion concentrations and membrane potential, as well as supporting figures are provided in the [Supporting Material](#). The source code of the model can be downloaded at <http://www.eheartsim.com>. In this section, the Ca^{2+} compartments, the distribution of ion channels and transporters within each compartment, the definition of nanodomain (*nd*), and modifications of the Hinch model are described.

Separation of Ca^{2+} compartments in the HuVEC model

Acsai et al. (12) found a higher $[\text{Ca}^{2+}]$ transient of 10–15 μM in a near releasing site (*nrs*). According to this finding, for our HuVEC model we divided the ion diffusion space (V_{cyt}) into three Ca^{2+} compartments (a junctional space (*jnc*), an intermediate zone (*iz*), and bulk space (*blk*), as indicated with different colors in Fig. 1):

$$V_{\text{cyt}} = V_{\text{jnc}} + V_{\text{iz}} + V_{\text{blk}}. \quad (1)$$

The cytosolic Ca^{2+} gradients were represented in three discrete steps by $[\text{Ca}^{2+}]_{\text{jnc}}$, $[\text{Ca}^{2+}]_{\text{iz}}$, and $[\text{Ca}^{2+}]_{\text{blk}}$. V_{jnc} was model adjusted to 0.8% of the apparent cell volume (V_{cell}) to give an appropriate bias level for $[\text{Ca}^{2+}]$ around Ca^{2+} -binding sites within a CaRU (denoted as $[\text{Ca}^{2+}]_{\text{nd}}$). The *iz* ($= 3.5\%$ of V_{cell}) defines an intermediate zone between *jnc* and *blk*, and may correspond to *nrs* in Acsai et al. (12).

The ion channels and transporters were distributed on the sarcolemma. I_{CaL} due to LCCs composing the CaRU at *nd* were assigned to *jnc*. To simulate CDI of whole-cell I_{CaL} , we assigned 75% of the LCCs to the *jnc*, 10% to *blk*, and the rest to *iz*. Other $[\text{Ca}^{2+}]$ -related currents, such as I_{Ks} , I_{Cab} , $I_{\text{L(Ca)}}$, I_{NCX} ($\text{Na}^+/\text{Ca}^{2+}$ exchanger), and I_{PMCA} , were distributed in *iz* (10%), and the rest of the currents were in *blk* (90%). All of the other channels and transporters were located in *blk*. The above assumption for NCX distribution seemed to be adequate for reconstructing the experimental recording of I_{NCX} evoked by the Ca^{2+} transient during 10- and 30-ms step pulses (12). Transferring half of the NCX from *iz* to *jnc* hardly affected the result because the $[\text{Ca}^{2+}]_{\text{jnc}}$ transient diminished too rapidly to evoke NCX effectively (the absence of NCX in rat dyad was previously reported (37), although its exact location is still uncertain (38)). No compartments were assumed for Na^+ and K^+ because their diffusion was estimated to be rapid (39,40), and all ion channels or transporters independent of Ca^{2+} were assigned to *cyt* for the sake of simplicity.

Nanodomain Ca^{2+} in the CaRU

To derive an expression for the $[\text{Ca}^{2+}]$ sensed by the LCCs and RyRs, we used the rapid equilibrium approximation adopted by Hinch (10) and Hinch et al. (11). In this approach, the calcium in the nanodomain ($[\text{Ca}^{2+}]_{\text{nd}}$) is assumed to be in an instantaneous steady state, since the time constant for equilibrium in this region is considerably smaller than the open times of the LCCs or RyRs, so that the efflux of calcium into the adjoining sink (*jnc* in this study) is balanced by the currents through the LCCs and RyRs. Using the same approximation, we can define $[\text{Ca}^{2+}]_{\text{nd}}$ as a function of $[\text{Ca}^{2+}]$ in two Ca^{2+} sources, SRrl ($[\text{Ca}^{2+}]_{\text{SRrl}}$) and extracellular space ($[\text{Ca}^{2+}]_o$), and in the Ca^{2+} sink compartment directly connected to *nd* ($[\text{Ca}^{2+}]_{\text{jnc}} = [\text{Ca}^{2+}]_{\text{oo}}$) and V_m :

$$[\text{Ca}]_{\text{nd}} = \frac{[\text{Ca}]_{\text{oo}} + f_R \times [\text{Ca}]_{\text{SRrl}} + f_L \times \frac{\delta V \cdot e^{-\delta V}}{1 - e^{-\delta V}} \times [\text{Ca}]_o}{1 + f_R + f_L \times \frac{\delta V}{1 - e^{-\delta V}}}, \quad (2)$$

$$f_R = 0.31, \quad f_L = 0.014,$$

where f_R ($=J_R/g_D$ (11) or $r_{\text{RyR}}/r_{\text{xfer}}$ (41)) and f_L ($=J_L/g_D$ (11) or $P_{\text{LCC}}/(V_{\text{ds}} \times r_{\text{xfer}})$ (41)) indicate the conductivity ratio between influx (flux from

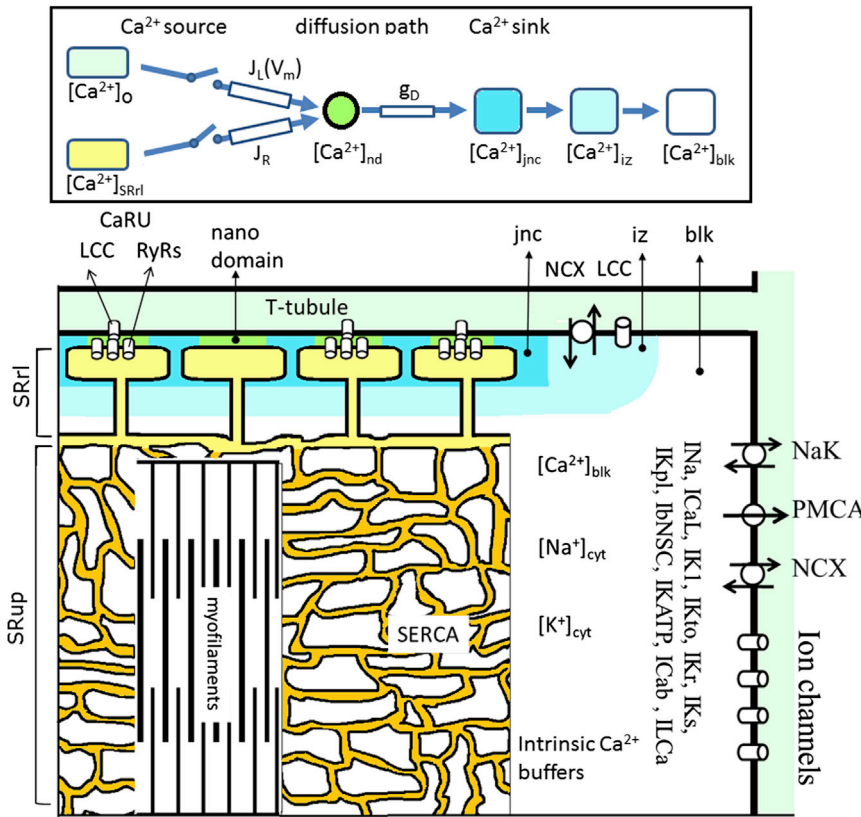


FIGURE 1 Composition of the HuVEC model demonstrated by a half-sarcomere. The compartments of *jnc*, *iz*, and *blk* in the cytosol, SR, and T-tubule are filled with different colors. The ion channels and transporters are located on the sarcolemma, SERCA and RyRs are on the SR membrane, and the contractile fibers are in *blk*. A single CaRU consists of a hypothetical LCC and a couplon in the junctional cleft (filled with green color), and individual CaRUs are spatially separated from their neighbors by *jnc*. The inset at the top shows a schematic presentation of the diffusion pathway of Ca^{2+} from the Ca^{2+} sources to the sink. J_L , J_R , and g_D represent the permeability of single LCCs and RyRs, and the Ca^{2+} flux rate from *nd* to *jnc*, respectively. The myofibrils were embedded in an SR network (SRup). I_{CaL} : L-type Ca^{2+} current; I_{Na} : sum of Na^+ currents in transient and late modes; $I_{NaT} + I_{NaL}$; I_{K1} : inward rectifier K^+ current; I_{Kr} : rapid component of delayed rectifier K^+ current; I_{Ks} : slow component of delayed rectifier K^+ current; I_{Kto} : transient outward K^+ current; I_{Kpl} : plateau K^+ current; $I_{I(Ca)}$: Ca^{2+} -activated background cation current; I_{Cab} : background Ca^{2+} current; I_{KATP} : ATP-sensitive K^+ current; I_{bNSC} : background nonselective cation current; NaK: Na^+/K^+ pump; NCX: Na^+/Ca^{2+} exchanger; PMCA: plasma membrane Ca^{2+} ATPase; SERCA: sarco-/endoplasmic reticulum Ca^{2+} pump.

a couplon and a hypothetical unit of several LCCs) and efflux (diffusion from *nd* to the Ca^{2+} sink compartment next to *nd*) within *nd*. δV stands for zFV_m/RT .

The first term of the numerator in Eq. 2, Ca_{00} , is the $[Ca^{2+}]$ in a functional Ca^{2+} compartment, *jnc* in the HuVEC model, which provides a direct sink of Ca^{2+} efflux from *nd* and is calculated by time integration of Ca^{2+} fluxes. The second and third terms of the numerator indicate components that are directly dependent on Ca^{2+} fluxes through a couplon or LCC, respectively. The instantaneous equilibrium of $[Ca^{2+}]_{nd}$ implies that *nd* is located on a diffusion pathway of Ca^{2+} fluxes from the source pools, i.e., the extracellular space for LCCs and the SRrI for couplons to a Ca^{2+} sink. Thus, $[Ca^{2+}]_{nd}$ takes an intermediate level between the millimolar level of $[Ca^{2+}]_o$ or $[Ca^{2+}]_{SR}$ in the source pool and the micromolar range in the sink pool. In this study, the sink pool of Ca^{2+} is defined as junctional space (*jnc*). Thus, $[Ca^{2+}]_{jnc}$ represents C_{00} in Eq. 2 and potentially is able to activate the CaRU in the absence of LCC activation, typically during a condition of Ca^{2+} overload of the SR. It should be noted that the $[Ca^{2+}]_{nd}$ has not been defined in the conventional cardiac cell models published to date, including the GPB and ORd models, but is frequently used to calculate the inactivation of LCCs in biophysical studies (26,28,30,42), as well as in the single couplon model of CICR with (43) or without (22,23) LCCs. The NL contraction model of Negroni and Lascano (44) was used without modification.

Modification of the state-transition scheme in the Hinch model

We modified the original Hinch model in three ways. First, the rapid inactivation step of RyR was removed. This was because inactivation occurred too slowly (34,35,45), and CICR termination had been reproduced in the absence of this inactivation state in the SJ, LC, and SM models. The activation and deactivation rates of a RyR were determined based on

single-channel recordings obtained experimentally. Second, the state transition to activate a couplon was separated into a triggering step and the subsequent regenerative activation step of RyRs, as was previously done for the full-stochastic SJ, LC, and SM models. In these models, the triggering step by LCCs was replaced simply by randomly opening one RyR (22,23). With regard to the gating properties of LCCs, we assumed that the V_m -dependent step and the Ca^{2+} -dependent step are independent of each other, as described in Shirokov et al. (26). We determined the rate constants of LCC kinetics by using experimental data obtained from HuVECs (Fig. S2). Third, we approximated the closing kinetics of a couplon based on the coincidence of simultaneous closing of multiple RyR openings.

After the modifications described above, CaRU kinetics could be expressed by an eight-state transition scheme as shown in Fig. 2. The gating of V_m -dependent and Ca^{2+} -dependent activations of LCCs and couplon activation are indicated along the *x*, *y*, and *z* axes, respectively. The probability of occupying a functional state of CaRU (*Y*) is denoted as Y_{xyz} , where subscripts *x*, *y*, and *z* indicate open (O) or closed (C). The four kinds of $[Ca^{2+}]_{nd}$ (Ca_{00} , Ca_{L0} , Ca_{0R} , and Ca_{LR}) calculated by Eq. 2 regulate the Ca^{2+} -mediated state transition along the *y* and *z* axes. When L or R is closed, the subscript for $[Ca^{2+}]_{nd}$ becomes 0 and the corresponding value of $[Ca^{2+}]_{nd}$ is calculated by nullifying J_L or J_R , respectively, in Eq. 2. The Y_{CCt} , COt , OCt or OOt defined by the subscript *t* in the functional state of *Y* indicates the probability of a triggered state, driven by Ca_{L0} or Ca_{00} as indicated in the scheme. Note that the regenerative step was determined by Ca_{L0} and Ca_{LR} for Y_{000} and by Ca_{00} and Ca_{0R} for the conformation states Y_{CO0} , Y_{CC0} , and Y_{OCC} of CaRU.

Determination of couplon kinetics

The opening (k_{co}) and closing (k_{oc}) rate constants of RyR determined from the single RyR recordings under physiologically relevant conditions are variable in the literature (46) (Fig. S5). In this study, we adopted the rate

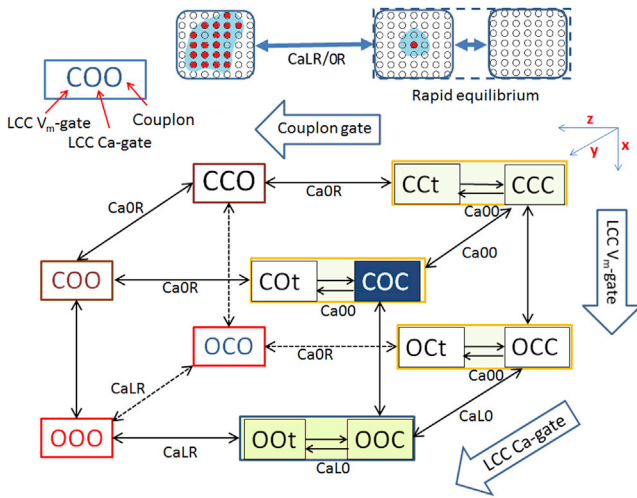


FIGURE 2 Scheme of the state transitions of the CaRU model (see text for further explanation). The inset shown at the top is a schematic illustration of a cluster of RyRs corresponding to the closed, triggered, and activated states of a couplon from right to left, respectively. Circles filled with red are open RyRs and open circles are closed ones. The blue stretch in the vicinity of open RyRs is an image of spreading Ca^{2+} . The first activation of a single RyR within a couplon is achieved either by Ca^{2+} influx through an activated LCC or by a spontaneous increase in $[\text{Ca}^{2+}]_{\text{ind}}$ during various Ca^{2+} -overload conditions.

constants used by Stern et al. (23), who referred to measurements by Guo et al. (47), to facilitate a comparison between the HuVEC model and the SM toy model. We adjusted the rates for temperature by introducing a temperature factor ($Q_{10} = 3$) after introducing a Hill equation for Ca^{2+} binding:

$$k_{co} = Q_{10} \times \frac{0.4}{1 + \left(\frac{0.025}{[\text{Ca}]_{\text{ind}}}\right)^{2.7}} \quad (3)$$

$$k_{oc} = Q_{10} \times 0.118 \times 4.8. \quad (4)$$

The original k_{oc} (0.118 ms^{-1}) was multiplied by 4.8, referring to k_{oc} used in previous CICR models (see Fig. S5).

For the triggering step of opening a single RyR by an adjacent LCC or spontaneously, an instantaneous equilibrium was assumed, and the probability of the triggered state (f_t) of a couplon was given by

$$f_t = \frac{k_{co}}{k_{co} + k_{oc}}. \quad (5)$$

In the regenerative step, an increasing number of RyRs are activated through nearest-neighbor activation by Ca^{2+} release within a couplon, as previously demonstrated in a full-stochastic simulation by Laver et al. (22) (see their Fig. 2). For practical purposes, this mechanism was approximated by a two-state transition model between full-open and closed states of a couplon. The forward rate k_{rco} and backward rate k_{roc} of the regenerative step were determined from the single-channel RyR kinetics k_{co} and k_{oc} by Eqs. 6 and 7:

$$k_{rco} = f_n \times f_t \times k_{co} \times (sloc0 + [\text{Ca}^{2+}]_{\text{SRrl}}) \quad (6)$$

$$k_{roc} = k_{oc} \cdot pC^{(N_{\text{RyR}}-1) \cdot l} \quad \text{where} \quad pC = \frac{k_{oc}}{k_{oc} + k_{co}}. \quad (7)$$

The factor f_n in Eq. 6 is a multiplying factor ($= 7$ in the HuVEC model) to express the spread of Ca^{2+} to activate nearest-neighbor RyRs within a couplon in the regenerative step. The last factor of Eq. 6 is adopted from the original SM model. Equation 7 is an empirical formula deduced by conducting a stochastic simulation of open-closed-state transitions of a number ($N_{\text{RyR}} = 10$) of individual RyRs within a couplon, defining a closed event of couplon with simultaneous closure of all RyRs. The pC is a steady-state probability of the closed conformation of a RyR. The l ($= 0.74$) is a correcting factor for the probability of simultaneous closure of $(N_{\text{RyR}} - 1)$ RyRs. Thus, k_{roc} decreases as k_{co} increases with increasing $[\text{Ca}^{2+}]_{\text{ind}}$. The lifetime of open events measured in the stochastic simulation agreed well with the k_{roc} determined by Eq. 7 at $N_{\text{RyR}} = 1-20$ or at various $[\text{Ca}^{2+}]_{\text{ind}}$. For further explanation, see ‘‘Determination of the deactivation rate of a couplon’’ in Supporting Materials and Methods.

The rate of change in the open probability of a couplon (pO) in a two-state transition model is then expressed as follows:

$$\frac{dpO}{dt} = k_{rco} \times (1 - pO) - k_{roc} \times pO. \quad (8)$$

We validated the overall activation and deactivation rates by performing a stochastic simulation of couplon activity (Fig. S6). Assuming the existence of 20,000 couplons in a whole cell, we observed 196 open events within 1000 ms, which is comparable to the 100 sparks/s reported for rat cardiac myocytes at a whole-cell level at rest (48).

RESULTS

Excitation and contraction in our presented HuVEC model

The new, to our knowledge, HuVEC model was able to restore a stable cycle of activity whenever the cycle length (CL) of stimulation was altered within the range examined (0.25–3 Hz; Fig. S9). A single cycle of activity is demonstrated in Fig. 3 A at a standard CL of 1000 ms. Fig. 3 A1 shows the control AP (black trace) and the AP after complete I_{Kr} block (red trace). The shape and the APD₉₀ of these APs are quite comparable to those reported in Jost et al. (49) in both the control and during the I_{Kr} block: APD₉₀ was prolonged from 291 to 424 ms (46% increase) as compared with 278–433 ms (56% increase) in Jost et al. (49). The standard AP parameters are comparable to those reported in ventricular myocytes (see the legend of Fig. 3 for references). The major plateau currents were I_{CaL} , I_{NaL} , and I_{NCX} in the inward direction (Fig. 3 A5), and I_{K1} , I_{Kto} , I_{Kpl} , I_{Kr} , I_{Ks} , and I_{NaK} in the outward direction (Fig. 3 A4). In Fig. 3 A2, $[\text{Ca}^{2+}]_{\text{SRrl}}$ (green) rapidly decreased from ~ 0.69 to a minimum level of ~ 0.04 mM, and $[\text{Ca}^{2+}]_{\text{SRup}}$ (chocolate) increased during the increase in $[\text{Ca}^{2+}]_{\text{blk}}$. The recovery of $[\text{Ca}^{2+}]_{\text{SRrl}}$ (green in Fig. 3 A2) was relatively slow during the AP because of the remaining small open probability of couplons due to incomplete CDI of I_{CaL} , as indicated by the plateau level of $[\text{Ca}^{2+}]_{\text{iz}}$ ($\sim 1.15 \mu\text{M}$) at ~ 200 – 300 ms in Fig. 3 A6 (black). After repolarization, the voltage gate of LCC was totally closed by ~ 350 ms (black in Fig. 3 A5), and $[\text{Ca}^{2+}]_{\text{SRrl}}$ (green in Fig. 3 A2) smoothly recovered during the diastolic period as a result of the Ca^{2+} supply from SR_{up} . The peak magnitudes of the Ca^{2+} transient were 106.3, 11.1, and $0.49 \mu\text{M}$ in *jnc*

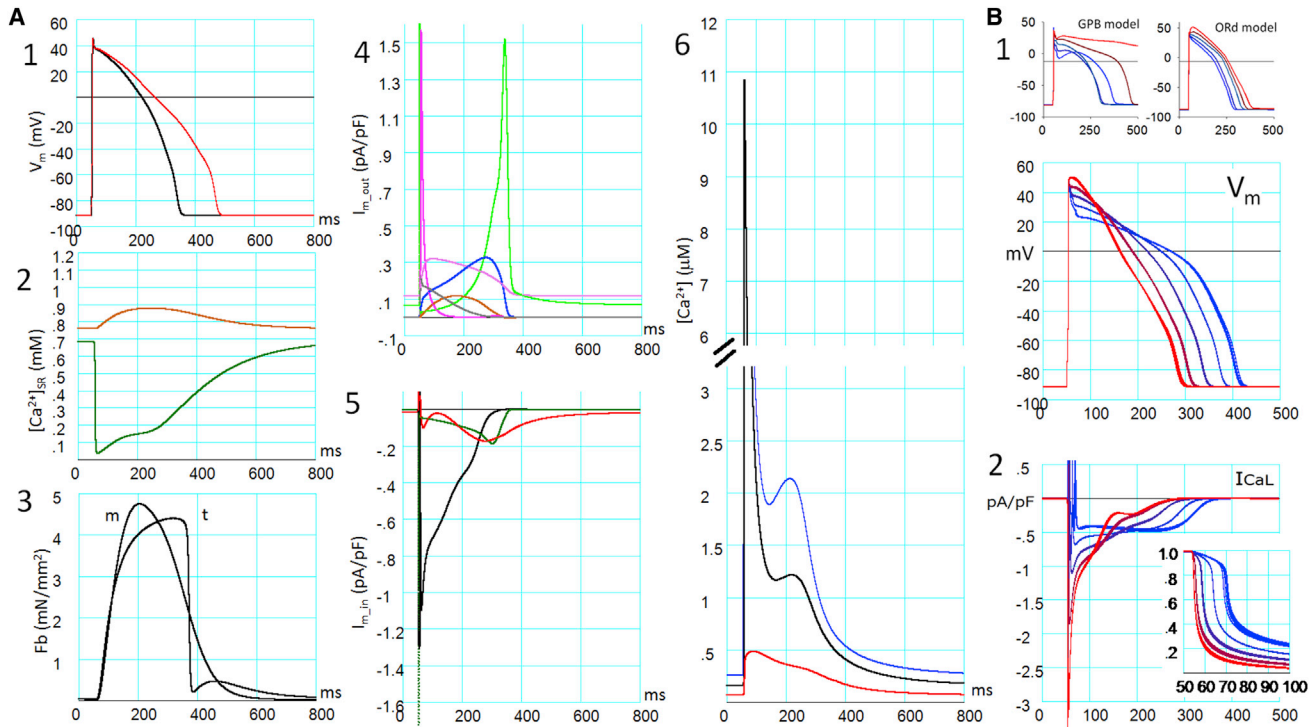


FIGURE 3 (A and B) A standard AP in the HuVEC model (A) and the effects of increased $[Ca^{2+}]_o$ on the AP and I_{CaL} (B). The AP was evoked by a 3-ms current injection at 50 ms. When stabilized at CL = 1000 ms, the AP parameters were measured. (A1, the resting potential) Approximately -91.4 mV (-84 mV (50), -81 mV (51), -87 mV (52)); maximum rate of rise of the AP: 244 Vs^{-1} (comparable to that in Péréon et al. (52)); duration at 90% repolarization (APD₉₀): 287 ms (300 ms (51,53,54)); and the plateau of V_m immediately after phase 1 repolarization: $\sim +37.7$ mV. The red AP was obtained when I_{Kr} was completely suppressed in a separate protocol. (A2) $[Ca^{2+}]_{SRup}$ (chocolate) and $[Ca^{2+}]_{SRrel}$ (green). (A3) Isotonic F_b at 6 mN/mm² (trace showing the delayed peak, t) and isometric F_b at 0.91 μ m half sarcomere length (m) in mN/mm². (A4) Outward current components (I_{Kto} (magenta), I_{Kr} (blue), I_{Ks} (chocolate), I_{K1} (yellow-green), I_{Kpl} (gray), and I_{NaK} (pink)). (A5) Inward current components (I_{NaL} (dark green), I_{CaL} (black), and I_{NCX} (red)). The negative peak of I_{NaL} at the onset of the AP is off the scale. I_{NaT} was not plotted. (A6) $[Ca^{2+}]_{jnc}$ (blue), $[Ca^{2+}]_{iz}$ (black), and $[Ca^{2+}]_{blk}$ (red). The large transient peak of $[Ca^{2+}]_{jnc}$ is off the scale and not shown. (B1) APs after a change in $[Ca^{2+}]_o$ are superimposed in the GPB and ORd models (top). Gradient colors from blue to red are coded in reference to $[Ca^{2+}]_o$, which was increased from 0.45 to 7.2 mM by a factor of 2. The same values for $[Ca^{2+}]_o$ were applied to the HuVEC model, and five AP traces were obtained after a change in $[Ca^{2+}]_o$ are superimposed (bottom). (B2) Traces of the I_{CaL} current and open probabilities of its Ca^{2+} -dependent inactivation gate (inset, with an expanded timescale) are shown using the same color code as in (B1).

(not shown), *iz* (black), and *blk* (red), respectively (Fig. 3 A6). The peak of developed tension (F_b) was quite delayed in the isotonic condition (t in Fig. 3 A3) compared with the isometric contraction (m in Fig. 3 A3), and relaxed quickly after the repolarization of AP in the NL contraction model (44).

The responses of the model cell to varying stimulus frequencies over the range of 0.25 – 3 Hz were examined and the results agreed well with the experimental findings as well as simulation results in both GPB and ORd models (for details, see Fig. S9).

CDI of I_{CaL} revealed by varying $[Ca^{2+}]_o$

The CDI of LCCs plays a pivotal role in regulating CICR. In our previous study (33), we confirmed that CDI was retarded by preventing SR Ca^{2+} release as demonstrated experimentally (12). Here, we further examined whether our CDI model, directly influenced by $[Ca^{2+}]_{nd}$ in the Hinch formu-

lation, could reproduce the other key experimental finding that an increase in $[Ca^{2+}]_o$ shortens the duration of the AP (APD), accompanied by a positive shift of the AP plateau potential (as observed in rabbit atrial cells (32) and guinea-pig ventricular cells (55)). As a result, changes in AP obtained by varying $[Ca^{2+}]_o$ to 0.45 , 0.9 , 1.8 , 3.6 and 7.2 mM in Fig. 3 B1 (+37, +20, 0, -17 , -35% change in APD measured at 50% repolarization, APD₅₀) agreed well with the experimental findings (+30, 0, -27% change in APD₅₀ by varying $[Ca^{2+}]_o$ to 0.62 , 2.5 , and 10.0 mM (32), and +45, 0, -22% change in APD₅₀ by varying $[Ca^{2+}]_o$ to 0.01 , 1.8 , 5.4 mM (55)), although the results were obtained in different animals. It was evident that CDI was accelerated with increasing $[Ca^{2+}]_o$ as shown by the open probability of the Ca^{2+} -dependent inactivation gate in Fig. 3 B2 (inset). In contrast, APD was elongated with increasing $[Ca^{2+}]_o$ in the GPB and ORd models, as shown in Fig. 3 B1. It should be noted that previous models mostly failed to reconstruct this APD shortening with

increasing $[Ca^{2+}]_o$, except for those developed by Matsuoka et al. (56) and Grandi et al. (57), and the APD shortening effect was much smaller in those models compared with the HuVEC model. In the Hinch formulation of CaRU kinetics, the CDI of LCCs is determined by $[Ca^{2+}]_{nd}$, which is directly related to $[Ca^{2+}]_o$ when the LCC is open (Eq. 2), and this in turn increases the CDI rate ε_+ of LCCs (Eq. S5).

Initiation and termination of CICR during the AP

The state transitions of CaRU during the entire time course of an AP are shown together with V_m in Fig. 4, A and B. The transitions during the initial 15 ms of the AP are shown in Fig. 4 C on an expanded timescale. Just before the AP, ~99.2% of CaRUs were in Y_{coc} (dark green) and the rest (0.8%) were in Y_{ccc} (lime), indicating that the V_m gate of LCC and the couplon gate were almost completely closed. At the onset of the AP, LCC was maximally activated to Y_{ooc} (chocolate, step 1 in Fig. 4, inset). The subsequent rapid opening of couplons (steps 2 and 3) is represented by transient peaks of Y_{ooo} (red) and Y_{oco} (blue) in Fig. 4 C. The peak time in Y_{oco} (blue, step 3) was only slightly delayed because CDI of LCCs is rapid ($< \sim 1$ ms). Since the V_m gate of LCC was continuously open, $Y_{c oo}$ (magenta) and Y_{cco} (yellow) scarcely appeared during the AP. The couplons closed through these rapid state transitions, and the closed conformation of couplons, Y_{occ} (gray), peaked at ~100 ms after the AP onset. During the subsequent repolarizing phase shown in Fig. 4, A and B, Y_{occ} (gray) was replaced by Y_{ccc} (lime) due to closure of the V_m gate of LCC (step 5). Finally, during diastole, the removal of CDI gradually proceeded to complete the recovery from Y_{ccc} (lime) to Y_{coc} (dark green) (arrow 6 in Fig. 4, inset).

Role of the feedback loop in determining the time courses of initiation and termination of CICR

To identify key factors in determining the activation time course of a couplon in HuVEC model, the eight-state transition scheme in Fig. 4 (inset) was reduced to a two-state scheme of couplon kinetics (Fig. 5, inset A). The overall activation and deactivation rates, $\overline{k_{rco}}$ and $\overline{k_{roc}}$, in this reduced scheme are given by a sum of the four activation rates ($k_{xyc \cdot xyo}$) and deactivation rates ($k_{xyo \cdot xyc}$) weighted by the probability (Y_{xyc} and Y_{xyo}) of staying in each state of the couplon:

$$\overline{k_{rco}} = \frac{k_{coc \cdot coo} \times Y_{coc} + k_{ooo \cdot ooc} \times Y_{ooc} + k_{occ \cdot oco} \times Y_{occ} + k_{ccc \cdot cco} \times Y_{ccc}}{Y_{coc} + Y_{ooc} + Y_{occ} + Y_{ccc}}$$

$$\overline{k_{roc}} = \frac{k_{c oo \cdot coc} \times Y_{c oo} + k_{ooo \cdot ooc} \times Y_{ooo} + k_{oco \cdot occ} \times Y_{oco} + k_{cco \cdot ccc} \times Y_{cco}}{Y_{c oo} + Y_{ooo} + Y_{oco} + Y_{cco}} \quad (9)$$

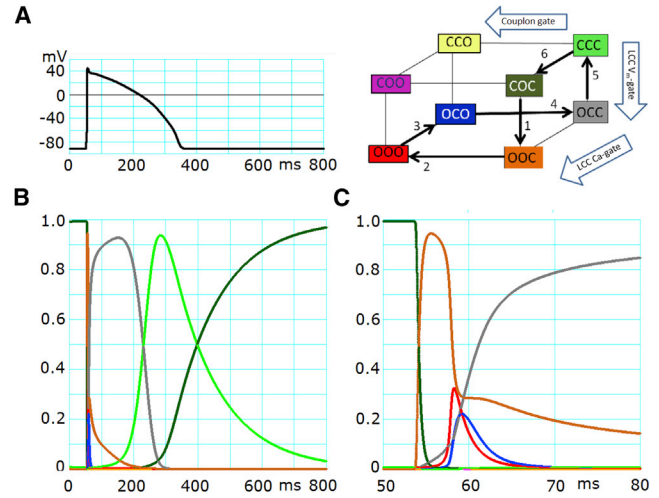


FIGURE 4 State transitions of CaRU during the AP. (A) The AP was triggered by a 3-ms current injection at 50 ms. (B) The probability of each state of CaRU is plotted on the same timescale as in (A) (ms). Each trace color indicates the state of CaRU of the corresponding color in the inset. Arrows 1–6 in the inset show the direction of major fluxes of the CaRU state transition after onset of the AP. (C) The time courses of the same state probabilities as in (A) are plotted on an expanded timescale for the initial period of 50–80 ms.

The rate constants $k_{xyc \cdot xyo}$ and $k_{xyo \cdot xyc}$ are given by Eqs. 6 and 7. The deactivation rate $\overline{k_{roc}}$ transiently decreased due to decreases in pC when $[Ca^{2+}]_{nd}$ was increased by activation of the couplon. An instantaneous equilibrium open probability of a couplon, pO_{eq} , is then calculated by the following equation, using $[Ca^{2+}]_{jnc}$, $[Ca^{2+}]_{SRnl}$, and V_m at each time step of the time integration throughout the time course of $pO(t)$:

$$pO_{eq} = \frac{\overline{k_{rco}}}{\overline{k_{rco}} + \overline{k_{roc}}} \quad (10)$$

Fig. 5 shows the time-dependent variables involved in determining $\overline{k_{rco}}$ and $\overline{k_{roc}}$, such as V_m (Fig. 5 A), $[Ca^{2+}]_{SRnl}$ (Fig. 5 B), and the four kinds of $[Ca^{2+}]_{nd}$ (Fig. 5 C) on a common expanded timescale, in addition to the time course of $\overline{k_{rco}}$ and $\overline{k_{roc}}$ (Fig. 5 D). In Fig. 5 E, it is evident that $pO(t)$ (red trace) always follows pO_{eq} (blue) with a time constant τ :

$$\frac{dpO(t)}{dt} = \frac{pO_{eq} - pO(t)}{\tau} \quad (11)$$

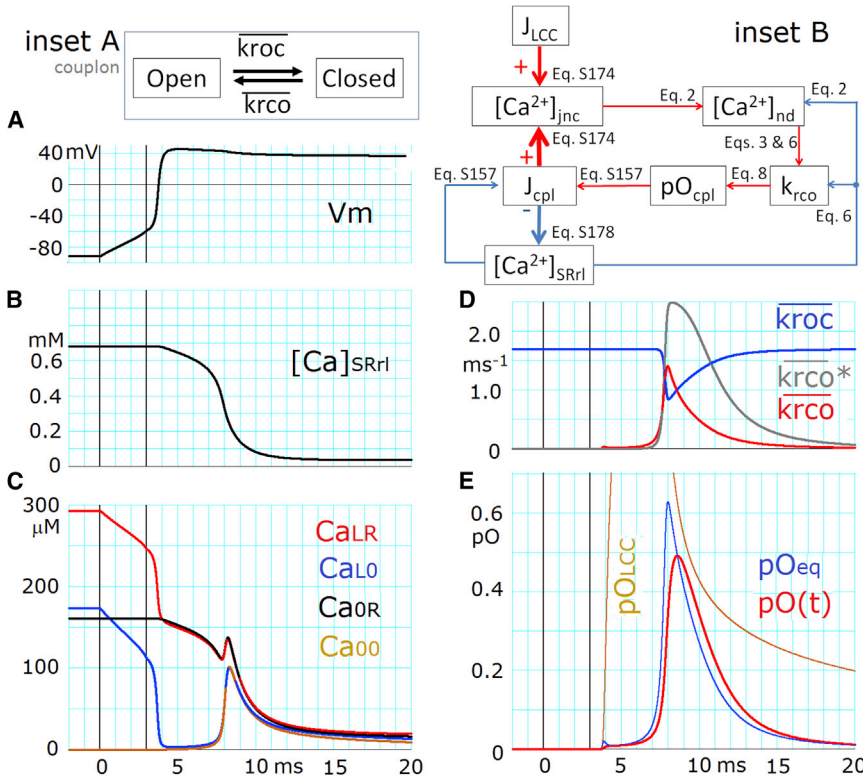


FIGURE 5 Activation and deactivation of couplons determined by the positive-feedback mechanism. (A) AP. (B) $[Ca^{2+}]_{SRrI}$. (C) $[Ca^{2+}]_{nd}$ (Ca_{LR} , Ca_{L0} , Ca_{OR} , and Ca_{00}). The dotted curves of CaLR, CaL0, and CaOR indicate that they are theoretical values and have virtually no influence on the kinetics, since both the couplon and LCC are mostly closed during this period. (D) The overall activation rate (\bar{k}_{rc0}) and deactivation rate (\bar{k}_{rc0}^*) of the couplon and k_{rc0}^* were obtained after fixing $[Ca^{2+}]_{SRrI}$ to a control value. (E) $pO(t)$ ($= Y_{000} + Y_{c00} + Y_{o00} + Y_{c00}$, red), and pO_{eq} and pO_{LCC} ($Y_{000} + Y_{o00}$; the peak is off the scale). The two vertical lines in all panels indicate the onset and offset of the stimulus current pulse. Inset A shows the reduced two-state transition of a couplon. Inset B shows the feedback loop formed by the five time-dependent variables, connected by five red arrows with equation numbers. The thick red and blue arrows indicate each Ca^{2+} release flux, which directly increases or decreases $[Ca^{2+}]_{jnc}$ or $[Ca^{2+}]_{SRrI}$, respectively.

$$\tau = \frac{1}{\bar{k}_{rc0} + \bar{k}_{roc}}. \quad (12)$$

In other words, whether CICR will develop ($pO_{eq} > pO(t)$) or terminate ($pO_{eq} < pO(t)$) is decided by the movement of pO_{eq} . Fig. 5, inset B, shows the sequence of interactions among time-dependent variables involved in determining the time course of open probability of a couplon, pO_{cpl} (pO_{eq} or $pO(t)$), with corresponding equations.

At the onset of an AP, LCC is immediately and almost fully activated (pO_{LCC} in Fig. 5 E, chocolate trace). However, the rapid increasing phase in pO_{cpl} (Fig. 5 E, red or blue) occurred with a significant delay of ~ 4.5 ms after the onset of LCC activation. This delay is caused by the fact that the magnitude of I_{CaL} largely decreases when V_m shifts from the resting potential toward more positive potentials. The magnitude of Ca_{L0} rapidly decreases along the AP onset (blue trace in Fig. 5 C, and the minimum value is $3.35 \mu M$ at ~ 4.5 ms), and thus Ca_{L0} fails to trigger an immediate regenerative activation of the couplon. The low Ca_{L0} , however, activates a small but gradually increasing number of CaRUs, and thus the Ca^{2+} fluxes through couplons cause a delayed time-dependent increase in jnc ($[Ca^{2+}]_{jnc} = Ca_{00}$, chocolate in Fig. 5 C). During a delay of ~ 4.5 ms, this Ca^{2+} accumulation progressively increases \bar{k}_{rc0} to generate a rapidly rising foot in pO_{cpl} . In Fig. 5, inset B, the variables connected by red arrows (pO_{cpl} , J_{cpl} , $[Ca^{2+}]_{jnc}$, $[Ca^{2+}]_{nd}$ and k_{rc0}) compose a posi-

tive-feedback loop, which evokes the exponential activation of pO_{eq} and thus $pO(t)$.

On the other hand, $[Ca^{2+}]_{SRrI}$ gradually decays during 4–8 ms because of increasing Ca^{2+} release from the SR (Fig. 5 B). This decay in $[Ca^{2+}]_{SRrI}$ tends to interfere with the enhancements of \bar{k}_{rc0} in the positive-feedback loop, mainly by decreasing three parameters: 1) the factor ($sloc0 + [Ca^{2+}]_{SRrI}$) in Eq. 6; 2) $[Ca]_{nd}$, as indicated in Fig. 5 C (Eq. 2); and 3) J_{cpl} ($J_{Ca_{rel}}$ in Eq. S157 in Supporting Materials and Methods). The net balance between the competitive effects of increasing $[Ca^{2+}]_{jnc}$ and decreasing $[Ca^{2+}]_{SRrI}$ on the positive-feedback loop is positive during the rising phase (5–8 ms) and reverses its sign in the falling phase of CICR (>9 ms).

It should be noted that these findings are entirely consistent with the results of full-stochastic simulations of CICR in a single CaRU (22,23) showing that CICR termination is driven by the feedback loop between a decrease in $[Ca^{2+}]$ in the dyadic cleft and n_{open} (in analogy to the decreasing $[Ca^{2+}]_{jnc}$ and pO_{cpl} in the HuVEC model). Indeed, the $[Ca^{2+}]_{jnc}$ (Ca_{00} in Eq. 2) is a major factor in determining $[Ca^{2+}]_{nd}$ after the start of regenerative couplon activation (Fig. 5 C). The rising phase of activation of $pO(t)$ (Fig. 5 E, red), lasting for only a few milliseconds, is also in good agreement with that observed in the full-stochastic simulation by Laver et al. (22).

To examine the influence of the last factor in Eq. 6, the ($sloc0 + [Ca^{2+}]_{SRrI}$) was fixed to a control value ($= 0.7337$ mM) before stimulus onset (Fig. 5 D). The

appearance of the rising foot was slightly retarded, but the activation rate (k_{rco}^*) was enlarged significantly by this intervention (*gray curve*), and the deactivation time course was prolonged, indicating that the factor ($sloc0 + [Ca^{2+}]_{SRnl}$) indeed decelerates activation and enhances the termination of CICR.

Graded Ca^{2+} release during voltage clamp in the ventricular cell model

In the feedback loop (Fig. 5, inset B), the component $[Ca^{2+}]_{jnc}$ is common to all CaRUs in the HuVEC model. Thus, Ca^{2+} accumulation in *jnc* may compromise the graded Ca^{2+} release in voltage-clamp experiments. This possibility was examined as shown in Fig. 6. Test depolarizing pulses were applied at 2 mV increments from a holding potential of -50 mV. I_{CaL} was activated in the usual voltage-dependent manner. In proportion to I_{CaL} activation, the peak amplitudes of Y_{ooo} increased (Fig. 6, B and E, graph 1). At strong depolarizations, Y_{ooo} also appeared with increasing peak amplitude through CDI of LCC (Fig. 6, B and E, graph 3). In addition, Y_{ooo} was activated with a markedly delayed time course of activation at negative potentials (Fig. 6 E, graph 4). The concomitant time evolution of Y_{ooo} with Ca_{00} ($= [Ca^{2+}]_{jnc}$) (Fig. 6 F) indicated that this activation of Y_{ooo} was largely due to the state transition from Y_{oc} to Y_{ooo} evoked by the $[Ca^{2+}]_{jnc}$ accumulation.

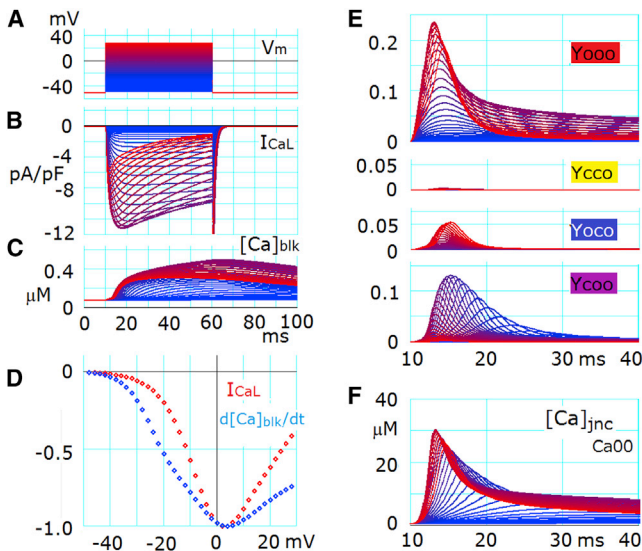


FIGURE 6 Graded Ca^{2+} release evoked by voltage-clamp pulses. (A) Voltage-clamp pulses for 50 ms were applied from a holding potential of -50 mV to various depolarized levels, from -38 to $+30$ mV, in increments of 2 mV. All recordings in all panels except for (D) are plotted with gradient colors from blue to red, coded in reference to the test potentials shown in (A). (B) Whole-cell I_{CaL} . (C) $[Ca^{2+}]_{blk}$. (D) The voltage relationship of peak I_{CaL} (red) and peak $d[Ca^{2+}]_{blk}/dt$ (blue) was recorded with test pulses in 2 mV increments, normalized by each peak value. (E) Time evolution of Y_{ooo} , Y_{cco} , Y_{oco} , and Y_{coo} . (F) Ca^{2+} accumulation in *jnc* is represented by Ca_{00} .

At more positive test potentials, the peak of Y_{ooo} decreased because an increasing number of CaRUs were activated by the V_m -dependent LCC activation pathway as observed during the AP, i.e., the same mechanism as indicated in Fig. 4 C and arrows 1–4 in the inset during the AP.

To examine the influence of this CaRU activation through an increase in $[Ca^{2+}]_{jnc}$, we plotted the relationship between the test potential and the peak of $d[Ca^{2+}]_{blk}/dt$ together with the peak I_{CaL} - V_m relation after normalizing to their peaks as in a previous experimental study (7) (Fig. 6 D). It is evident that the HuVEC model captures key properties of the graded Ca^{2+} release even in the presence of local Ca^{2+} accumulation. The time courses of Ca^{2+} transients in *blk* evoked by each clamp pulse are superimposed in Fig. 6 C. One might be able to resolve the difference in the relationship between the dependencies of $d[Ca^{2+}]_{blk}/dt$ and I_{CaL} on V_m in the positive V_m range in the HuVEC model from experiment (7) by conducting voltage-clamp experiments under controlled levels of $[Ca^{2+}]_{SRnl}$.

DISCUSSION

Mathematical analysis of couplon activation

CICR in the HuVEC model is based on biophysical mechanisms to a much larger extent than that in previous human or animal cell models, which mostly used the conventional common-pool model of CICR. Here, the CICR mechanisms are compared with the models specified for CICR rather than with other whole-cell models.

The two crucial and innovative assumptions in the tightly coupled LCC-RyR kinetic model (Hinch model) remain intact in our revised model. First, the compound kinetic states of the CaRU are defined by combinations of three different gates: the V_m -dependent and Ca^{2+} -dependent gates of LCCs, and the activation gate of couplons. Second, the $[Ca^{2+}]_{nd}$ around the Ca^{2+} -binding sites for couplon activation and LCC inactivation is given by an instantaneous function of $[Ca^{2+}]$ in the two Ca^{2+} sources and the sink when the LCC and/or couplon are open (Eq. 2). To be consistent with the detailed stochastic models of CICR, however, the activation step of a couplon is separated into a triggering step and a regenerative step, which are driven by $[Ca^{2+}]_{nd}$, namely, Ca_{00} or Ca_{L0} , and Ca_{0R} or Ca_{LR} , respectively (Fig. 2). The deactivation kinetics is approximated based on the simultaneous closure of multiple RyRs within a couplon.

To reveal the mechanistic principle of CICR, we compared empirical equations among the models (see Table S6 for a comparison of explicit mathematical descriptions of the regenerative step). In the toy version of the SM model, they analytically deduced a deterministic solution of the activation rate by assembling individual reaction steps. In the SJ model, the cooperative factors CF_{open} and CF_{close} were simply defined for the regenerative activation of

RyRs and had a relatively small influence on the activation rate of a couplon (Fig. S5). In our modified Hinch model, we approximated the nearest-neighbor effect by using an activation rate (k_{rco}) that was sevenfold larger than the original single-channel rate (k_{co}) (f_n in Eq. 6), and k_{co} was accelerated with increasing $[Ca^{2+}]_{nd}$ (Eqs. 3 and 6). Thus, in all three models, the activation of a couplon was reduced to a two-state transition scheme. In both the SM and HuVEC models, the equilibrium open probability, pO_{eq} , of a couplon was examined. Stern et al. (23) disclosed an unstable equilibrium pO_{eq} (= number of open RyRs (n_{open})/number of total RyRs (n_{ry})) at a given $[Ca^{2+}]_{SRr}$ and successfully defined a threshold pO_{eq} for both the activation and termination of couplon activity. The HuVEC model revealed that an instantaneous pO_{eq} leads to time-dependent changes in $pO(t)$, and that $[Ca]_{jnc}$ and $[Ca]_{SRr}$ are time-dependent factors that are responsible for varying pO_{eq} (or k_{rco}) via Eqs. 3, 6, and 10. Thus, the core feedback loop (Fig. 5, inset B) is fully consistent with the view that the initiation and termination of CICR is determined by mechanisms analogous to those suggested in recent stochastic models. In the future, investigators should analyze quantitative aspects of the threshold phenomenon systematically using mathematical approaches, such as bifurcation or phase-plane analyses, to gain deeper insights into the biophysical mechanisms that underlie excitation-contraction coupling in the HuVEC model.

Verification of assuming *jnc* and *iz*

In the HuVEC model, incorporation of *jnc* and *iz* into the CICR model was a prerequisite to represent the exponential Ca^{2+} gradient by discrete $[Ca^{2+}]$ steps around the Ca^{2+} -releasing site during CICR. However, such a Ca^{2+} gradient near $[Ca^{2+}]_{nd}$ or $[Ca^{2+}]_{ds}$ was not included in the original Hinch model ($Ca_{00} = [Ca^{2+}]_{cyr}$ in Eq. 2), and Ca_{L0} was much lower than in the HuVEC model. Therefore, an activation rate constant larger than the experimental rate by more than two to three orders of magnitude was used (22,47) (see Fig. S5). This difficulty is overcome by the high $[Ca^{2+}]_{nd}$ biased by the local Ca_{00} ($= [Ca^{2+}]_{jnc}$) in the HuVEC model. Furthermore, we found that the Ca_{L0} was still too low to evoke an immediate activation of couplons by I_{CaL} (Fig. 5 C), even when we used the sevenfold larger rate constant. This is because of the sharp V_m -dependent decrease of Ca_{L0} at the AP plateau potential (Eq. 2). It turned out that the $[Ca^{2+}]_{jnc}$ in the very limited volume of *jnc* was progressively increased even by the infrequent openings of couplons to generate the foot of rapid activation of couplons through the positive-feedback loop (Fig. 5, inset B).

The presence of *jnc* was a key factor in reproducing the experimental APD shortening with increasing $[Ca^{2+}]_o$. Fig. 3 B reveals enhanced CDI of LCC with increasing $[Ca^{2+}]_o$ underlying the APD shortening. Indeed, ~90% of

CDI occurred within the initial 50 ms, during which time the peak $[Ca^{2+}]_{jnc}$ was higher by ~9-fold than the peak $[Ca^{2+}]_{iz}$, which may be comparable to $[Ca^{2+}]$ in the subsarcolemmal spaces of the GPB or Ord models. The presence of *jnc* was also essential in evoking DAD in the HuVEC model, as has been demonstrated elsewhere (33).

In a previous study, Wier et al. (7) made the interesting finding that although a brief I_{CaL} tail current observed on repolarization from +80 mV to the holding potential (-40 mV) subsided within ~2 ms, the decay of the Ca^{2+} transient due to J_{cpl} continued with a half-time of ~9 ms at the holding potential. In our HuVEC model, this delayed closure of couplons after a brief I_{CaL} tail ($t_{1/2} = 0.9$ ms, the time to reach half of the maximum amplitude from the off time of the test pulse) was well simulated by the rate of $[Ca^{2+}]_{jnc}$ decay ($t_{1/2} = 4.4$ ms), which was attributed to the delayed diffusion of the accumulated Ca^{2+} from *jnc* to *iz* and *blk*. Since no space was assumed for Ca^{2+} accumulation in the original Hinch model, the Ca^{2+} transient evoked by RyR activation should closely follow the time course of the I_{CaL} tail with a maximum delay of ~1 ms, as determined by k_{oc} of RyR.

Taken together, the above findings justify the incorporation of *jnc* into the HuVEC model.

Ca^{2+} compartments: *jnc*, *iz*, SR_r , and SR_{up}

The $[Ca^{2+}]_{nrs}$ measured by Acsai et al. (12) was assigned to a functional space rather than a histologically defined one (58). When this large Ca^{2+} gradient was introduced into the HuVEC model, *nrs* was further divided into two hypothetical spaces, *iz* and *jnc*, and $[Ca^{2+}]_{jnc}$ was used to represent Ca_{00} in the Hinch formalism of $[Ca^{2+}]_{nd}$ (Eq. 2). Then, the volume of *jnc* was adjusted to reconstruct the key experimental and simulation results described above. Since the time course of CICR is largely determined by the size of *jnc*, V_{jnc} is compared with the volume of dyadic space (V_{ds}), which is also critical for CICR kinetics in the stochastic simulations of a single CaRU. As shown in Table 1, the V_{jnc} in our model is apparently larger than the V_{ds} assumed in other CICR models, but the difference is relatively small compared with the upper limit of V_{ds} in the LC model. Considering the effects of fixed buffer sites on membrane phospholipids or the Debye layer, the Ca^{2+} distribution volume of *ds* may increase dramatically, as indicated in Stern et al. (23). The effective size of the compartment depends on various factors, such as the kinetics of the buffers (dissociation constants), the number of available binding sites, and the membrane surface area that encloses this compartment, but not on the myoplasmic volume that it encloses (58). Therefore, it is always important to evaluate the functional volume of each compartment comprehensively.

Since $[Ca^{2+}]_{SRr}$ is one of central factors in driving the controlled termination of CICR (Fig. 5, inset B), we also compared V_{SRr} among different models together with

TABLE 1 Comparison of the Volumes of Junctional Ca²⁺ Compartments and [CSQN]_{SRrl} among the Models

	SJ Model	LC Model	SM Model	HuVEC Model
V_{ds} or V_{jnc} in the HuVEC model	0.002–0.005 ^a pL/cell 1.0×10^{-7} pL for each d.s.	0.0486–0.1215 ^a pL/cell 2.43×10^{-6} pL for each d.s.	0.013–0.033 ^a pL/cell cleft height 30 nm, $(7 \times 30)^2$ nm ² area for each d.s.	0.303 pL/cell 0.8% V_{cell}
V_{SRrl}	0.2–0.5 ^a pL/cell 1.0×10^{-5} pL for each CaRU	0.08–0.21 ^a pL/cell 4.21×10^{-6} pL for each CaRU	0.14 pL/cell 0.35% V_{cell} assumed in the HuVEC model	0.46 pL/cell 1.2% V_{cell}
[CSQN] _{SRrl}	10.0 mM	30.0 mM	30.0 mM	3 mM
V_{SRup}	infinite	3.5% V_{cell}	3.5% V_{cell}	4.8% V_{cell}

In the Hinch model, 50,000 CaRUs/cell and 2×10^{-7} pL/d.s. were assumed.

^aCalculated by assuming 20,000–50,000 CaRUs/cell.

[CSQN]_{SRrl} (Table 1). Although V_{SRrl} in the HuVEC model is ~4-fold larger than the corresponding size of junctional SR in the SM model, it may be concluded that the Ca²⁺-releasing potency of the SR-releasing site is similar between the two, because 10-fold smaller Ca²⁺ buffering power is assumed in the HuVEC model compared with the SM model. Indeed, if the number of CaRUs within a cell is assumed to be 50,000 as in the Hinch model, V_{SRrl} values in the SJ and LC models are within the same range as in the HuVEC model when a larger [CSQN]_{SRrl} in each model is taken into account.

The extent of Ca²⁺ depletion in SRrl depends not only on V_{SRrl} but also on the kinetics of V_{SRrl} refilling and couplon gating. The time constant for the refilling of V_{SRrl} in the HuVEC model is ~200 ms, which is in agreement with that previously reported for rabbit (59). It should be noted, however, that the refilling time course and Ca²⁺ mobility in the SR varies between different studies (59,60). The recovery time course of local Ca²⁺ depletion, the so-called blink, is also variable between different studies (61,62). Furthermore, the separation of the SR volume into V_{SRrl} and V_{SRup} is still largely conventional and has not been explicitly determined based on experimental findings.

Limitations of the CICR model presented here

The HuVEC model successfully reproduced both electrical activity and Ca²⁺ dynamics, which were very similar to those observed in intact cells. However, the mathematical mechanisms developed in this model cell may not necessarily be a unique solution for intact cells. One limitation of the model is due to the large variety in the gating kinetics of RyRs (Fig. S5). Furthermore, if the functional size of SR Ca²⁺ compartments near the Ca²⁺-releasing site can be established experimentally, the model will be greatly improved and enhance our understanding of the effects of local SR Ca²⁺ depletion. To test the possibility that local SR Ca²⁺ depletion, which is responsible for terminating individual couplon open events, is engaged in terminating CICR at a whole-cell level, we formulated a dyadic model with a blink space (*bs*) in addition to the Hinch formalism (see Supporting Materials and Methods for a theoretical treatment of *bs*). Our preliminary simulation using this

dyadic model with *bs* suggested that the general behavior of the model was essentially the same in electrically stimulated activity and voltage-clamp experiments.

Under pathophysiological conditions, Ca²⁺ waves spontaneously occur and propagate in myocytes. This Ca²⁺ wave cannot be reproduced in our HuVEC model because it has a single space of *jnc* and SRrl. Furthermore, in a previous study, Matsuda et al. (63) suggested that asynchronous CICR occurs spontaneously in multiple domains of the SR network within a single cell (for a simulation, see Chen et al. (64)). In that study, Matsuda et al. found that micro fluctuations remained in the recordings of the resting potential after several cyclic DAD events subsided, and suggested multiple origins of the spontaneous Ca²⁺ release with variable intrinsic rhythms under the condition of Ca²⁺ overload. Nonetheless, the assumption of common [Ca²⁺]_{jnc} and [Ca²⁺]_{SRrl} might be relevant in our simulations as long as the activation of all of the CaRUs within the cell are synchronized by an AP or a voltage-clamp pulse. To refine the CICR model, it may be necessary to conduct voltage-clamp experiments under controlled levels of [Ca²⁺]_{SRrl} (58).

SUPPORTING MATERIAL

Supporting Materials and Methods, Supporting Results, nine figures, and six tables are available at [http://www.biophysj.org/biophysj/supplemental/S0006-3495\(15\)00599-8](http://www.biophysj.org/biophysj/supplemental/S0006-3495(15)00599-8).

AUTHOR CONTRIBUTIONS

A.N. designed the study. A.N., K.A., C.Y.C., H.M., and Y.H. performed research and developed the HuVEC model. A.N., Y.H., A.A., and K.A. analyzed the model and wrote the manuscript with T.P.

ACKNOWLEDGMENTS

We thank Drs. T. Shimayoshi and Y. Takeda for fruitful discussions.

This work was supported by Grants-in-Aid from the Ministry of Education, Culture, Sports, Science and Technology of Japan (22590216 to C.C. and 22390039 to A.N.), a Grant-in-Aid for JSPS Fellows from the Japan Society for the Promotion of Science (to Y.H.), Program for Application of the Grants-in-Aid for Scientific Research (KAKENHI) (to Y.H.), and the Ritsumeikan-Global Innovation Research Organization at Ritsumeikan University.

SUPPORTING CITATIONS

References (65–90) appear in the Supporting Material.

REFERENCES

- Priebe, L., and D. J. Beuckelmann. 1998. Simulation study of cellular electric properties in heart failure. *Circ. Res.* 82:1206–1223.
- Ten Tusscher, K. H., O. Bernus, ..., A. V. Panfilov. 2006. Comparison of electrophysiological models for human ventricular cells and tissues. *Prog. Biophys. Mol. Biol.* 90:326–345.
- ten Tusscher, K. H., D. Noble, ..., A. V. Panfilov. 2004. A model for human ventricular tissue. *Am. J. Physiol. Heart Circ. Physiol.* 286:H1573–H1589.
- Grandi, E., F. S. Pasqualini, and D. M. Bers. 2010. A novel computational model of the human ventricular action potential and Ca transient. *J. Mol. Cell. Cardiol.* 48:112–121.
- O'Hara, T., L. Virág, ..., Y. Rudy. 2011. Simulation of the undiseased human cardiac ventricular action potential: model formulation and experimental validation. *PLOS Comput. Biol.* 7:e1002061.
- Volders, P. G., A. Kulcsár, ..., B. Szabo. 1997. Similarities between early and delayed afterdepolarizations induced by isoproterenol in canine ventricular myocytes. *Cardiovasc. Res.* 34:348–359.
- Wier, W. G., T. M. Egan, ..., C. W. Balke. 1994. Local control of excitation-contraction coupling in rat heart cells. *J. Physiol.* 474:463–471.
- Stern, M. D. 1992. Theory of excitation-contraction coupling in cardiac muscle. *Biophys. J.* 63:497–517.
- Greenstein, J. L., and R. L. Winslow. 2002. An integrative model of the cardiac ventricular myocyte incorporating local control of Ca²⁺ release. *Biophys. J.* 83:2918–2945.
- Hinch, R. 2004. A mathematical analysis of the generation and termination of calcium sparks. *Biophys. J.* 86:1293–1307.
- Hinch, R., J. L. Greenstein, ..., R. L. Winslow. 2004. A simplified local control model of calcium-induced calcium release in cardiac ventricular myocytes. *Biophys. J.* 87:3723–3736.
- Acsai, K., G. Antoons, ..., K. R. Sipido. 2011. Microdomain [Ca²⁺] near ryanodine receptors as reported by L-type Ca²⁺ and Na⁺/Ca²⁺ exchange currents. *J. Physiol.* 589:2569–2583.
- Adachi-Akahane, S., L. Cleemann, and M. Morad. 1996. Cross-signaling between L-type Ca²⁺ channels and ryanodine receptors in rat ventricular myocytes. *J. Gen. Physiol.* 108:435–454.
- Sipido, K. R., G. Callewaert, and E. Carmeliet. 1995. Inhibition and rapid recovery of Ca²⁺ current during Ca²⁺ release from sarcoplasmic reticulum in guinea pig ventricular myocytes. *Circ. Res.* 76:102–109.
- Trafford, A. W., M. E. Díaz, ..., D. A. Eisner. 1995. Comparison of subsarcolemmal and bulk calcium concentration during spontaneous calcium release in rat ventricular myocytes. *J. Physiol.* 488:577–586.
- Weber, C. R., K. S. Ginsburg, and D. M. Bers. 2003. Cardiac submembrane [Na⁺] transients sensed by Na⁺-Ca²⁺ exchange current. *Circ. Res.* 92:950–952.
- Weber, C. R., V. Piacentino, 3rd, ..., D. M. Bers. 2002. Na⁺-Ca²⁺ exchange current and submembrane [Ca²⁺] during the cardiac action potential. *Circ. Res.* 90:182–189.
- Cannell, M. B., and C. H. Kong. 2012. Local control in cardiac E-C coupling. *J. Mol. Cell. Cardiol.* 52:298–303.
- Stern, M. D., and H. Cheng. 2004. Putting out the fire: what terminates calcium-induced calcium release in cardiac muscle? *Cell Calcium.* 35:591–601.
- Zalk, R., S. E. Lehnart, and A. R. Marks. 2007. Modulation of the ryanodine receptor and intracellular calcium. *Annu. Rev. Biochem.* 76:367–385.
- Sobie, E. A., K. W. Dilly, ..., M. S. Jafri. 2002. Termination of cardiac Ca(2+) sparks: an investigative mathematical model of calcium-induced calcium release. *Biophys. J.* 83:59–78.
- Laver, D. R., C. H. Kong, ..., M. B. Cannell. 2013. Termination of calcium-induced calcium release by induction decay: an emergent property of stochastic channel gating and molecular scale architecture. *J. Mol. Cell. Cardiol.* 54:98–100.
- Stern, M. D., E. Ríos, and V. A. Maltsev. 2013. Life and death of a cardiac calcium spark. *J. Gen. Physiol.* 142:257–274.
- Brunet, S., T. Scheuer, and W. A. Catterall. 2009. Cooperative regulation of Ca(v)1.2 channels by intracellular Mg(2+), the proximal C-terminal EF-hand, and the distal C-terminal domain. *J. Gen. Physiol.* 134:81–94.
- Ferreira, G., J. Yi, ..., R. Shirokov. 1997. Ion-dependent inactivation of barium current through L-type calcium channels. *J. Gen. Physiol.* 109:449–461.
- Shirokov, R., R. Levis, ..., E. Ríos. 1993. Ca(2+)-dependent inactivation of cardiac L-type Ca2+ channels does not affect their voltage sensor. *J. Gen. Physiol.* 102:1005–1030.
- Yue, D. T., and E. Marban. 1990. Permeation in the dihydropyridine-sensitive calcium channel. Multi-ion occupancy but no anomalous mole-fraction effect between Ba2+ and Ca2+. *J. Gen. Physiol.* 95:911–939.
- Neher, E., and W. Almers. 1986. Fast calcium transients in rat peritoneal mast cells are not sufficient to trigger exocytosis. *EMBO J.* 5:51–53.
- Stern, M. D. 1992. Buffering of calcium in the vicinity of a channel pore. *Cell Calcium.* 13:183–192.
- Tadross, M. R., R. W. Tsien, and D. T. Yue. 2013. Ca2+ channel nanodomains boost local Ca2+ amplitude. *Proc. Natl. Acad. Sci. USA.* 110:15794–15799.
- Kokubun, S., M. Nishimura, A. Noma, and H. Irisawa. 1982. Membrane currents in the rabbit atrioventricular node cell. *Pflugers Arch.* 393:15–22.
- Seifen, E., H. Schaer, and J. M. Marshall. 1964. Effect of calcium on the membrane potentials of single pacemaker fibres and atrial fibres in isolated rabbits atria. *Nature.* 202:1223–1224.
- Asakura, K., C. Y. Cha, ..., A. Noma. 2014. EAD and DAD mechanisms analyzed by developing a new human ventricular cell model. *Prog. Biophys. Mol. Biol.* 116:11–24.
- Valdivia, H. H., J. H. Kaplan, ..., W. J. Lederer. 1995. Rapid adaptation of cardiac ryanodine receptors: modulation by Mg2+ and phosphorylation. *Science.* 267:1997–2000.
- Fill, M., A. Zahradníková, ..., S. Györke. 2000. Ryanodine receptor adaptation. *J. Gen. Physiol.* 116:873–882.
- Näbauer, M., and M. Morad. 1990. Ca2(+)-induced Ca2+ release as examined by photolysis of caged Ca2+ in single ventricular myocytes. *Am. J. Physiol.* 258:C189–C193.
- Scriven, D. R., P. Dan, and E. D. Moore. 2000. Distribution of proteins implicated in excitation-contraction coupling in rat ventricular myocytes. *Biophys. J.* 79:2682–2691.
- Scriven, D. R., and E. D. Moore. 2013. Ca²⁺ channel and Na⁺/Ca²⁺ exchange localization in cardiac myocytes. *J. Mol. Cell. Cardiol.* 58:22–31.
- Hille, B. 2001. *Ion Channels of Excitable Membranes*. Sinauer Associates, Sunderland, MA.
- Swietach, P., K. W. Spitzer, and R. D. Vaughan-Jones. 2015. Na⁺ ions as spatial intracellular messengers for co-ordinating Ca²⁺ signals during pH heterogeneity in cardiomyocytes. *Cardiovasc. Res.* 105:171–181.
- Greenstein, J. L., R. Hinch, and R. L. Winslow. 2006. Mechanisms of excitation-contraction coupling in an integrative model of the cardiac ventricular myocyte. *Biophys. J.* 90:77–91.
- Peterson, B. Z., J. S. Lee, ..., D. T. Yue. 2000. Critical determinants of Ca(2+)-dependent inactivation within an EF-hand motif of L-type Ca(2+) channels. *Biophys. J.* 78:1906–1920.

43. Williams, G. S., M. A. Huertas, ..., G. D. Smith. 2007. A probability density approach to modeling local control of calcium-induced calcium release in cardiac myocytes. *Biophys. J.* 92:2311–2328.
44. Negroni, J. A., and E. C. Lascano. 2008. Simulation of steady state and transient cardiac muscle response experiments with a Huxley-based contraction model. *J. Mol. Cell. Cardiol.* 45:300–312.
45. Györke, S., and M. Fill. 1993. Ryanodine receptor adaptation: control mechanism of Ca(2+)-induced Ca2+ release in heart. *Science.* 260:807–809.
46. Qin, J., G. Valle, ..., M. Fill. 2009. Ryanodine receptor luminal Ca2+ regulation: swapping calsequestrin and channel isoforms. *Biophys. J.* 97:1961–1970.
47. Guo, T., D. Gillespie, and M. Fill. 2012. Ryanodine receptor current amplitude controls Ca2+ sparks in cardiac muscle. *Circ. Res.* 111:28–36.
48. Cheng, H., W. J. Lederer, and M. B. Cannell. 1993. Calcium sparks: elementary events underlying excitation-contraction coupling in heart muscle. *Science.* 262:740–744.
49. Jost, N., L. Virág, ..., S. Nattel. 2013. Ionic mechanisms limiting cardiac repolarization reserve in humans compared to dogs. *J. Physiol.* 591:4189–4206.
50. Peeters, G. A., M. C. Sanguinetti, ..., W. H. Barry. 1995. Method for isolation of human ventricular myocytes from single endocardial and epicardial biopsies. *Am. J. Physiol.* 268:H1757–H1764.
51. Li, G. R., J. Feng, ..., M. Carrier. 1998. Transmural heterogeneity of action potentials and Ito1 in myocytes isolated from the human right ventricle. *Am. J. Physiol.* 275:H369–H377.
52. Péréon, Y., S. Demolombe, ..., D. Escande. 2000. Differential expression of KvLQT1 isoforms across the human ventricular wall. *Am. J. Physiol. Heart Circ. Physiol.* 278:H1908–H1915.
53. Li, G. R., J. Feng, ..., S. Nattel. 1996. Evidence for two components of delayed rectifier K+ current in human ventricular myocytes. *Circ. Res.* 78:689–696.
54. Drouin, E., F. Charpentier, ..., H. Le Marec. 1995. Electrophysiologic characteristics of cells spanning the left ventricular wall of human heart: evidence for presence of M cells. *J. Am. Coll. Cardiol.* 26:185–192.
55. Kokubun, S., and H. Irisawa. 1984. Effects of various intracellular Ca ion concentrations on the calcium current of guinea-pig single ventricular cells. *Jpn. J. Physiol.* 34:599–611.
56. Matsuoka, S., N. Sarai, ..., A. Noma. 2003. Role of individual ionic current systems in ventricular cells hypothesized by a model study. *Jpn. J. Physiol.* 53:105–123.
57. Grandi, E., F. S. Pasqualini, ..., S. Severi. 2009. Theoretical investigation of action potential duration dependence on extracellular Ca2+ in human cardiomyocytes. *J. Mol. Cell. Cardiol.* 46:332–342.
58. Livshitz, L., K. Acsai, ..., Y. Rudy. 2012. Data-based theoretical identification of subcellular calcium compartments and estimation of calcium dynamics in cardiac myocytes. *J. Physiol.* 590:4423–4446.
59. Picht, E., A. V. Zima, ..., D. M. Bers. 2011. Dynamic calcium movement inside cardiac sarcoplasmic reticulum during release. *Circ. Res.* 108:847–856.
60. Swietach, P., K. W. Spitzer, and R. D. Vaughan-Jones. 2008. Ca2+-mobility in the sarcoplasmic reticulum of ventricular myocytes is low. *Biophys. J.* 95:1412–1427.
61. Zima, A. V., E. Picht, ..., L. A. Blatter. 2008. Termination of cardiac Ca2+ sparks: role of intra-SR [Ca2+], release flux, and intra-SR Ca2+ diffusion. *Circ. Res.* 103:e105–e115.
62. Brochet, D. X., W. Xie, ..., W. J. Lederer. 2011. Quarky calcium release in the heart. *Circ. Res.* 108:210–218.
63. Matsuda, H., A. Noma, ..., H. Irisawa. 1982. Transient depolarization and spontaneous voltage fluctuations in isolated single cells from guinea pig ventricles. Calcium-mediated membrane potential fluctuations. *Circ. Res.* 51:142–151.
64. Chen, W., G. Aistrup, ..., Y. Shiferaw. 2011. A mathematical model of spontaneous calcium release in cardiac myocytes. *Am. J. Physiol. Heart Circ. Physiol.* 300:H1794–H1805.
65. Beuckelmann, D. J., M. Näbauer, and E. Erdmann. 1992. Intracellular calcium handling in isolated ventricular myocytes from patients with terminal heart failure. *Circulation.* 85:1046–1055.
66. Powell, T., M. F. Sturridge, ..., V. W. Twist. 1981. Intact individual heart cells isolated from human ventricular tissue. *Br. Med. J. (Clin. Res.).* 283:1013–1015.
67. Satoh, H., L. M. Delbridge, ..., D. M. Bers. 1996. Surface:volume relationship in cardiac myocytes studied with confocal microscopy and membrane capacitance measurements: species-dependence and developmental effects. *Biophys. J.* 70:1494–1504.
68. Jost, N., L. Virág, ..., A. Varró. 2005. Restricting excessive cardiac action potential and QT prolongation: a vital role for IKs in human ventricular muscle. *Circulation.* 112:1392–1399.
69. Sakakibara, Y., T. Furukawa, ..., J. A. Wasserstrom. 1993. Sodium current in isolated human ventricular myocytes. *Am. J. Physiol.* 265:H1301–H1309.
70. Mewes, T., and U. Ravens. 1994. L-type calcium currents of human myocytes from ventricle of non-failing and failing hearts and from atrium. *J. Mol. Cell. Cardiol.* 26:1307–1320.
71. Jost, N., L. Virág, ..., J. G. Papp. 1998. Delayed rectifier potassium current in undiseased human ventricular myocytes. *Cardiovasc. Res.* 40:508–515.
72. Gerdes, A. M., S. E. Kellerman, ..., D. D. Schocken. 1992. Structural remodeling of cardiac myocytes in patients with ischemic cardiomyopathy. *Circulation.* 86:426–430.
73. Shannon, T. R., F. Wang, ..., D. M. Bers. 2004. A mathematical treatment of integrated Ca dynamics within the ventricular myocyte. *Biophys. J.* 87:3351–3371.
74. Pelzmann, B., P. Schaffer, ..., B. Koidl. 1998. L-type calcium current in human ventricular myocytes at a physiological temperature from children with tetralogy of Fallot. *Cardiovasc. Res.* 38:424–432.
75. Magyar, J., N. Iost, ..., P. P. Nanasi. 2000. Effects of endothelin-1 on calcium and potassium currents in undiseased human ventricular myocytes. *Pflugers Arch.* 441:144–149.
76. Fülöp, L., T. Bányász, ..., P. P. Nánási. 2004. Reopening of L-type calcium channels in human ventricular myocytes during applied epicardial action potentials. *Acta Physiol. Scand.* 180:39–47.
77. Sun, L., J. S. Fan, ..., P. T. Palade. 2000. A model of the L-type Ca2+ channel in rat ventricular myocytes: ion selectivity and inactivation mechanisms. *J. Physiol.* 529:139–158.
78. Zhang, J. F., P. T. Ellinor, ..., R. W. Tsien. 1994. Molecular determinants of voltage-dependent inactivation in calcium channels. *Nature.* 372:97–100.
79. Matsuda, H. 1986. Sodium conductance in calcium channels of guinea-pig ventricular cells induced by removal of external calcium ions. *Pflugers Arch.* 407:465–475.
80. Yan, D. H., and K. Ishihara. 2005. Two Kir2.1 channel populations with different sensitivities to Mg(2+) and polyamine block: a model for the cardiac strong inward rectifier K(+) channel. *J. Physiol.* 563:725–744.
81. Ishihara, K., and D. H. Yan. 2007. Low-affinity spermine block mediating outward currents through Kir2.1 and Kir2.2 inward rectifier potassium channels. *J. Physiol.* 583:891–908.
82. Rajamani, S., L. L. Eckhardt, ..., C. T. January. 2006. Drug-induced long QT syndrome: hERG K+ channel block and disruption of protein trafficking by fluoxetine and norfluoxetine. *Br. J. Pharmacol.* 149:481–489.
83. Takeuchi, A., S. Tatsumi, ..., A. Noma. 2006. Ionic mechanisms of cardiac cell swelling induced by blocking Na+/K+ pump as revealed by experiments and simulation. *J. Gen. Physiol.* 128:495–507.
84. Oka, C., C. Y. Cha, and A. Noma. 2010. Characterization of the cardiac Na+/K+ pump by development of a comprehensive and mechanistic model. *J. Theor. Biol.* 265:68–77.

85. Smith, N. P., and E. J. Crampin. 2004. Development of models of active ion transport for whole-cell modelling: cardiac sodium-potassium pump as a case study. *Prog. Biophys. Mol. Biol.* 85:387–405.
86. Tran, K., N. P. Smith, ..., E. J. Crampin. 2009. A thermodynamic model of the cardiac sarcoplasmic/endoplasmic Ca(2+) (SERCA) pump. *Biophys. J.* 96:2029–2042.
87. Negroni, J. A., and E. C. Lascano. 1996. A cardiac muscle model relating sarcomere dynamics to calcium kinetics. *J. Mol. Cell. Cardiol.* 28:915–929.
88. Brochet, D. X., D. Yang, ..., H. Cheng. 2005. Ca²⁺ blinks: rapid nanoscopic store calcium signaling. *Proc. Natl. Acad. Sci. USA.* 102:3099–3104.
89. Li, G. R., B. Yang, ..., S. Nattel. 1999. Transmembrane ICa contributes to rate-dependent changes of action potentials in human ventricular myocytes. *Am. J. Physiol.* 276:H98–H106.
90. Pieske, B., B. Kretschmann, ..., G. Hasenfuss. 1995. Alterations in intracellular calcium handling associated with the inverse force-frequency relation in human dilated cardiomyopathy. *Circulation.* 92:1169–1178.

Supporting Material

A Human Ventricular Myocyte Model with a Refined Representation of Excitation-Contraction Coupling

Yukiko Himeno,¹ Keiichi Asakura,^{1,2} Chae Young Cha,^{1,3} Hiraku Memida,¹ Trevor Powell,⁴ Akira Amano,¹ and Akinori Noma¹

¹Biosimulation Research Center, College of Life Sciences, Ritsumeikan University,
Noji Higashi 1-1-1 Kusatsu-City, Shiga, Japan

²Nippon Shinyaku, Co., Ltd., 14, Nishinosho-Monguchi-cho, Kisshoin, Minami-ku, Kyoto, Japan

³Oxford Centre for Diabetes Endocrinology and Metabolism,
University of Oxford, Churchill Hospital, Oxford, OX3 7LJ, UK.

⁴Department of Pharmacology, University of Oxford, Oxford OX1 3QT, UK

The source code of the computer model can be downloaded at <http://www.eheartsim.com>.

Abbreviations

Table S1. Abbreviations in model equations

V_m	membrane potential (mV)
I_{tot_cell}	total current of ion channels and exchangers (pA/pF)
$I_{tot_X_a}$	total current of ion 'X' channels and exchangers at space 'a' (pA/pF)
I_{app_blk}	current applied through a patch electrode (pA/pF)
E_X	reversal potential of ion 'X', determined by the Nernst equation (mV)
C_m	Whole cell membrane capacitance (pF)

G_I	conductance of current 'I' (pA /pF/mV)
GHK_{X_a}	a modified Goldman-Hodgkin-Katz equation of ion 'X' at space 'a' (mM)
k, α, β, ν	rate constants (/ms)
K_{d_X}	dissociation constant for ion 'X' (mM)
$P_{I(X)}$	converting factor of current 'I' from GHK_X (pA/pF /mM)
ν_{cyc_T}	turnover rate of transporter 'T' (/ms)
$p(S)_{(a)}$	probability of state 'S' in a scheme of state transitions at space 'a'
V_X	total volume of space 'X' (pL)
$[X_{\text{total}}]_a$	total concentration of substance 'X' at space 'a' (mM)
$[X_{\text{free}}]_a$	free concentration of substance 'X' at space 'a' (mM)
$[X]_a$	concentration of 'X' at space 'a' (mM)
J_X	total flux of ion 'X' (amol/ms)
z_X	valence of ion 'X'
$\frac{d[X]_a}{dt}$	rate of change of 'X' concentration at space 'a' (mM/ms)

Model parameters

Physical constants

Table S2 Physical constants

R	8.3143	C·mV/mmol/K
T	310	K
F	96.4867	C/mmol

Ion concentrations

Table S3 Ionic composition of external solution

$[K^+]_o$	4.5	mM
$[Na^+]_o$	140	mM
$[Ca^{2+}]_o$	1.8	mM

Substrates (fixed)

Table S4. Substrates

[MgATP] _{cyt}	6.631	mM
[MgADP] _{cyt}	0.0260	mM
[Pi] _{cyt} (free form)	0.5087	mM
[H ⁺] _{cyt}	0.0001	mM
[Mg ²⁺] _{cyt}	0.8	mM
[SPM]	0.005	μM

GHK equation

The magnitudes of ion channel currents are described by the ohmic equation or by the GHK equation. In the latter case, the term to convert mM to pA (permeability times zF) in the original GHK equation is represented by a lumped converting factor, P in a unit of pA·mM⁻¹, because of unknown total number of channels within a cell and single channel ion permeability. Then, the fully-activated current amplitude (I) for an ion X is given by,

$$I = P \cdot GHK_X$$

where GHK_X is,

$$GHK_X = \frac{z_X F V_m}{RT} \cdot \frac{\left([X]_i - [X]_o \cdot \exp\left(\frac{-z_X F V_m}{RT}\right) \right)}{\left(1 - \exp\left(\frac{-z_X F V_m}{RT}\right) \right)}$$

Nernst equation

$$E_X = \frac{R \cdot T}{z_X \cdot F} \cdot \log\left(\frac{[X]_o}{[X]_i}\right)$$

Cell geometry and SR Ca²⁺ compartments

The cell configuration and scalability of the HuVEC model (Sc_Cell)

Almost all models of cardiac myocyte have been developed using a given input capacitance (C_m) and a whole cell volume (V_{cell}). However, the dissociated human ventricular myocytes show a large variety of both cell size (see Fig. 1 in (1)) and the input capacitance (C_m, Fig. S1) as has been obtained in other mammalian species (2). In the present study, we developed a cell model, which can maintain identical characteristics independently of the cell size. Since no human data are available for the relationship between V_{cell} and C_m, we referred to the data (red line in Fig. S1) obtained by Satoh et al., (3), who applied the three-dimensional volume rendering method of confocal images to dissociated rabbit, ferret and rat cells. Though the rat data showed a different slope, we used a slope of 0.197 pL/pF as a first approximation, which is similar to the experimental value of 0.215 pL/pF in both rabbit and ferret. The V_{cell}-C_m relationship (the red line in Fig. S1) was modified to meet the origin. A standard V_{cell} (V_{std} =

37.92 pL) and a C_m ($C_{std} = 192.46$ pF) were set at a medium size within the range of measurements in human ventricular cells, represented by a rectangular block with a standard size of $120 \times 37.62 \times 8.4 \mu\text{m}^3$, and an input capacitance of 192.46 pF. Note that the range of V_{cell} , calculated over the range of experimental C_m well overlaps with the experimental V_{cell} in Fig. S1. We confirmed that the characteristics of the cell remained unchanged if volume of intracellular Ca^{2+} compartments and rate of Ca^{2+} transfer between SR and the cytosol were scaled by a scaling factor, $Sc_Cell = C_m / C_{std}$, where C_m is the input capacitance measured in a ventricular cell used in experiments.

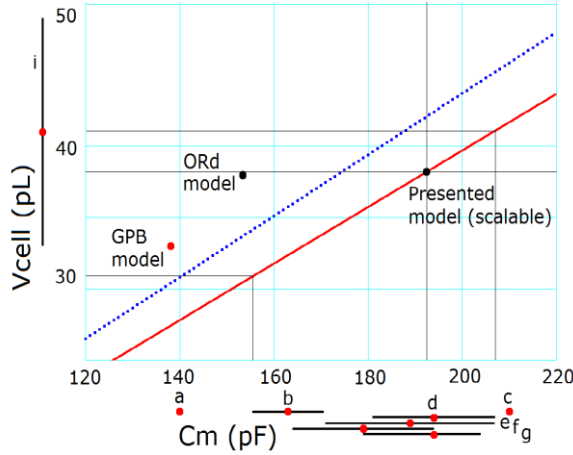


Fig. S1. Relationship between C_m and V_{cell} in the human ventricular cells.

Measurements of the input capacitance C_m of dissociated human ventricular myocyte in various references are indicated along the abscissa by mean values from 2 references (a; (1), c; (4)), or by mean \pm SEM from 5 references (b, (1), d; (5), e; (6), f; (7), g; (8)). An experimental measurement of V_{cell} in hearts with normal coronary arteries (9) is indicated with mean \pm SEM along the vertical axis. The cell size used in GPB (red point) and ORd (black point) models are indicated in comparison with the thick red line representing the relationship between the V_{cell} and C_m in HuVEC model, given by the following equation. The black point on the red line indicates the standard cell in the present study.

$$V_{cell} = \frac{37.92}{192.46} \cdot C_m$$

The experimental relationship in rabbit ventricular myocytes (3) is shown by the blue dotted line, which is given by,

$$V_{cell} = 0.215 \cdot C_m + 0.718$$

Table S5 compares the volumes of cell as well as Ca^{2+} compartments in HuVEC model with GPB and ORd models. The total volume of SR was set at 6% of V_{cyt} as in ORd model. The volume of SR_{ri} in HuVEC model was adjusted based on two premises [1] $[\text{Ca}^{2+}]_{\text{SRri}}$ decreases to less than $\sim 10\%$ of the diastolic level during CICR as assumed in the previous studies (10, 11) in the presence of 3 mM calsequestrin (2.6 and 10 mM in GPB and ORd model, respectively), and [2] CICR results in a peak amplitude of $\sim 0.5 \mu\text{M}$ for the global Ca^{2+} transients in the presence of Ca^{2+} uptake by SERCA and myoplasmic Ca^{2+} buffers including troponin, calmodulin, ATP as well as fixed binding sites on the T-tubule and SR membranes as in GPB model.

Table S5 Cell geometry compared with previous models

	GPB model	ORd model	HuVEC model
Cell configuration (cell volume)	(V_{cell}) Cylinder $L = 100 \mu\text{m}$, $r = 10.25 \mu\text{m}$ (= 33 pL)	(V_{cell}) Cylinder $L = 100 \mu\text{m}$, $r = 11 \mu\text{m}$ (= 38 pL)	(V_{cell}) Scalable rectangular block $L = 120 \mu\text{m}$, $W = 37.62 \mu\text{m}$, $D = 8.4 \mu\text{m}$ (= 37.92 pL)
Bulk space	(V_{myo}) 65% V_{cell} (= 21.45 pL)	(V_{myo}) 68% V_{cell} (= 25.84 pL)	(V_{blk}) 68% V_{cell} (= 25.79 pL)
Total SR space	(V_{sr}) 3.5% V_{cell} (= 1.16 pL)	(V_{sr}) 6% V_{cell} (= 2.28 pL)	(V_{sr}) 6% V_{cell} (= 2.28 pL)
SR releasing site volume	-	(V_{jsr}) 0.48 % V_{cell} (= 0.182 pL)	(V_{SRrl}) 1.2 % V_{cell} (= 0.46 pL)
SR uptake site volume	-	(V_{nsr}) 5.52 % V_{cell} (= 2.098 pL)	(V_{SRup}) 4.8 % V_{cell} (= 1.82 pL)
Junction space	(V_{junc}) 0.0539 % V_{cell} (= 0.0178 pL)	-	($V_{jnc} + V_{nd}$) 0.8 % V_{cell} (= 0.30 pL)
Subsarcolemmal space	(V_{sl}) 2% V_{cell} (= 0.66 pL)	(V_{ss}) 2 % V_{cell} (= 0.76 pL)	(V_{iz}) 3.5 % V_{cell} (= 1.33 pL)
Diffusion conductivity	$G_{Ca_{slmyo}} = 3724 \text{ fL/ms}$	$G_{dca_{ssmyo}} = 3800 \text{ fL/ms}$	$G_{dCa_{jnciz}} = 3396 \text{ fL/ms}$ and $G_{dCa_{izblk}} = 3508 \text{ fL/ms}$
Input capacitance	138.1 pF	153.4 pF	192.46 pF

Ca²⁺ buffer

The detailed set of buffer species (12) used in the GPB model was adopted after several simplifications as described in our previous paper (13). In short, we deleted the myosin, Na⁺ and Mg²⁺ buffers, and fixed [Mg²⁺]. The low affinity binding of Ca²⁺ to troponin (TnCl) was replaced by a contraction model (14) and the amount of the high affinity site (TnCh) was adjusted.

Bulk space (*blk*)

$$\frac{d[CaMCa]}{dt} = k_{on_CaM} \cdot [Ca^{2+}]_{blk} \cdot ([B_{total}CaM] - [CaMCa]) - k_{off_CaM} \cdot [CaMCa]$$

$$k_{off_CaM} = 0.238, k_{on_CaM} = 34$$

$$\frac{d[TnChCa]}{dt} = k_{on_TnCh} \cdot [Ca^{2+}]_{blk} \cdot ([B_{total}TnCh] - [TnChCa]) - k_{off_TnCh} \cdot [TnChCa]$$

$$k_{off_TnCh} = 0.000032, k_{on_TnCh} = 2.37$$

$$\frac{d[SRCa]}{dt} = k_{on_SR} \cdot [Ca^{2+}]_{blk} \cdot ([B_{total}SR] - [SRCa]) - k_{off_SR} \cdot [SRCa]$$

$$k_{off_SR} = 0.06, k_{on_SR} = 100$$

Intermediate zone (iz)

$$[L_{free}]_{iz} = \frac{[B_{total}L]_{iz}}{1 + \frac{[Ca^{2+}]_{iz}}{K_{dL_{iz}}}}$$

$$K_{dL_{iz}} = \frac{k_{off_L_{iz}}}{k_{on_L_{iz}}}, k_{off_L_{iz}} = 1.3, k_{on_L_{iz}} = 100$$

$$[H_{free}]_{iz} = \frac{[B_{total}H]_{iz}}{1 + \frac{[Ca^{2+}]_{iz}}{K_{dH_{iz}}}}$$

$$K_{dH_{iz}} = \frac{k_{off_H_{iz}}}{k_{on_H_{iz}}}, k_{off_H_{iz}} = 0.03, k_{on_H_{iz}} = 100$$

$$[Ca^{2+}]_{iz} = \frac{[Ca_{tot}]_{iz}}{1 + \frac{[Lf]_{iz}}{K_{dL_{iz}}} + \frac{[Hf]_{iz}}{K_{dH_{iz}}}}$$

Junctional space (jnc)

$$[L_{free}]_{jnc} = \frac{[B_{total}L]_{jnc}}{1 + \frac{[Ca^{2+}]_{jnc}}{K_{dL_{jnc}}}}$$

$$K_{dL_{jnc}} = \frac{k_{off_L_{jnc}}}{k_{on_L_{jnc}}}, k_{off_L_{jnc}} = 1.3, k_{on_L_{jnc}} = 100$$

$$[H_{free}]_{jnc} = \frac{[B_{total}H]_{jnc}}{1 + \frac{[Ca^{2+}]_{jnc}}{K_{dH_{jnc}}}}$$

$$K_{dH_{jnc}} = \frac{k_{off_H_{jnc}}}{k_{on_H_{jnc}}}, k_{off_H_{jnc}} = 0.03, k_{on_H_{jnc}} = 100$$

$$[Ca^{2+}]_{jnc} = \frac{[Ca_{tot}]_{jnc}}{1 + \frac{[Lf]_{jnc}}{K_{dL_{jnc}}} + \frac{[Hf]_{jnc}}{K_{dH_{jnc}}}}$$

Release site of the SR (SRr)

$$K_{d_CSQN_Ca} = \frac{k_{off_CSQN}}{k_{on_CSQN}}$$

$$k_{off_CSQN} = 65, k_{on_CSQN} = 100$$

$$a = 1$$

$$b = [B_{total}CSQN] - [Ca^{2+}]_{SRr} + K_{d_CSQN_Ca}$$

$$c = -K_{d_CSQN_Ca} \cdot [Ca^{2+}]_{SRr}$$

$$[Ca^{2+}]_{SRr} = \frac{-b + \sqrt{b^2 - 4 \cdot a \cdot c}}{2 \cdot a}$$

Boundary Ca²⁺ diffusion

Ca²⁺ transfer between cytosolic compartments

$$J_{Ca_jnciz} = G_{dCa_jnciz} \cdot ([Ca^{2+}]_{jnc} - [Ca^{2+}]_{iz}) \cdot Sc_Cell$$

$$G_{dCa_jnciz} = 3395.88 \text{ (fL} \cdot \text{ms}^{-1}\text{)}$$

$$J_{Ca_izblk} = G_{dCa_izblk} \cdot ([Ca^{2+}]_{iz} - [Ca^{2+}]_{blk}) \cdot Sc_Cell$$

$$G_{dCa_izblk} = 3507.78 \text{ (fL} \cdot \text{ms}^{-1}\text{)}$$

Ca²⁺ transfer from SR uptake site to release site

$$J_{trans_SR} = P_{trans} \cdot ([Ca^{2+}]_{SRup} - [Ca^{2+}]_{SRri}) \cdot Sc_cell$$

$$P_{trans} = 4.8037$$

Ion channels and transporters

L-type Ca²⁺ current (I_{CaL}, LCC)

We used the scheme of Shirokov *et al.* (1993) and Ferreira *et al.* (1997), in which Ca²⁺, passing through the channel itself, takes the primary role in the Ca²⁺-mediated inactivation (15-18). The same 4-state model was used for both LCCs in CaRU (I_{CaL_jnc}) and for LCCs located in *iz* (I_{CaL_iz}) and *blk* (I_{CaL_blk}). The [Ca²⁺]_{nd} determined by Eqs. 2 or S150-S153 were used to calculate the Ca²⁺-mediated inactivation for I_{CaL_jnc}, and [Ca²⁺]_{nd} determined by Eqs. S175, S176 for I_{CaL_iz} and I_{CaL_blk}. This [Ca²⁺]_{nd} is ~10 times-higher than the average [Ca²⁺]_{jnc} in HuVEC or [Ca²⁺] in the Ca²⁺ compartments ([Ca²⁺]_{jnc} in GPB or [Ca²⁺]_{ss} in GPB models) obtained by the time-integration of fluxes in the cleft space in most of cardiac cell models. The rate constants for the V_m-gate (α₊ and α₋) and Ca²⁺-gate (ε₊ and ε₋) of LCC are given by Eqs. S1, S2 and Eqs. S5, S6, respectively. Both of the activation (α₊) and deactivation (α₋) rates of the V_m-gate were described as a function of two exponential terms, and adjusted to human data (see activation curve (chocolate) superimposed on experimental data in Fig. S2A, B).

$$\alpha_+ = \frac{1}{3.734 \cdot \text{Exp}\left(-\frac{V_m}{8.5}\right) + 0.35 \cdot \text{Exp}\left(-\frac{V_m}{3500}\right)} \quad (\text{Eq. S1})$$

$$\alpha_- = \frac{1}{4.65 \cdot \text{Exp}\left(\frac{V_m}{15}\right) + 1.363 \cdot \text{Exp}\left(\frac{V_m}{100}\right)} \quad (\text{Eq. S2})$$

The rate constant (ε₊) for the Ca²⁺-inactivation was determined according to the Hinch algorithm. The inactivation rate ε₊ could be divided into two terms by integrating Eq. S3 with S4.

$$\tilde{\alpha}_+ = \frac{\exp\left(\frac{V_m - V_L}{\Delta V_L}\right)}{t_L \cdot \left(\exp\left(\frac{V_m - V_L}{\Delta V_L}\right) + 1\right)} \quad (\text{Eq. S3})$$

$$\tilde{\varepsilon}_+ = \frac{[Ca^{2+}]_{nd} \cdot (\exp(\frac{V_m - V_L}{\Delta V_L}) + a)}{\tau_L \cdot \tilde{K}_L (\exp(\frac{V_m - V_L}{\Delta V_L}) + 1)} = \frac{[Ca^{2+}]_{nd} \cdot t_L \cdot \tilde{\alpha}_+}{\tau_L \cdot \tilde{K}_L} + \frac{[Ca^{2+}]_{nd} \cdot a}{\tau_L \cdot \tilde{K}_L (\exp(\frac{V_m - V_L}{\Delta V_L}) + 1)} \quad (\text{Eq. S4})$$

where V_L is defined as a potential when half LCC open, ΔV_L width of opening potentials, t_L time switching between C and O states, τ_L , inactivation time, K_L concentration at inactivation and a biasing to make inactivation function of V. To avoid confusion, α , ε and K_L from Hinch model were given a tilde. The first term of Eq. S4 is a function of both $[Ca^{2+}]_{nd}$, the activation rate of V_m -gate ($\tilde{\alpha}_+$) and V_m . The second term is a sigmoidal function of V_m , increasing with increasing negativity of V_m toward a saturation level, unlikely in experiments. Therefore, the second term was removed for simplicity, and Eq. S5 was used in our model.

$$\varepsilon_+ = \frac{[Ca^{2+}]_{nd} \cdot \alpha_+}{T_L \cdot K_L}, \quad (\text{Eq. S5})$$

where α_+ is given by Eq. S1 and τ_L/t_L in Eq. S4 was substituted by T_L .

$$T_L = 147.51$$

In the revised model, the values of T_L ($= 147.51$) and K_L ($= 0.0044$ mM) (or the product of $T_L \times K_L$) for ε_+ , and a new equation for ε_- (Eq. S5 and S6) were determined by referring to the experimental measurements of steady-state inactivation (Fig. S2_B) and time constants (Fig. S2_C3) described in literatures (see legends of Fig. S2 for references). The value of $[Ca^{2+}]_{nd}$ (Ca_{L0} , or Ca_{LR}) shown in Fig. S2C1 was determined by Eq. S152 or S153, respectively, at a representative $[Ca^{2+}]_{SRfl}$ of 0.7 mM and a $[Ca^{2+}]_{jnc}$ of 0.0001 mM. The ε_+ was calculated at four different values of $[Ca]_{SRfl}$ (0.71, 0.51, 0.31, 0.11 mM) as shown in Fig. S2_B and S2_C, since $[Ca]_{SRfl}$ might be different in experimental conditions and thereby caused variations in the data of I_{CaL} inactivation. The rate of removing Ca^{2+} inactivation (ε_-) was determined by referring to the recovery rate from the inactivation at the resting potential in Fig. S2C3 and the V_m -dependence of steady-state inactivation in B.

$$\varepsilon_- = \frac{1}{8084 \cdot \text{Exp}(\frac{V_m}{10}) + 158 \cdot \text{Exp}(\frac{V_m}{1000})} + \frac{1}{134736 \cdot \text{Exp}(-\frac{V_m}{5}) + 337 \cdot \text{Exp}(-\frac{V_m}{2000})} \quad (\text{Eq. S6})$$

The $[Ca^{2+}]_{nd}$ for LCC located in *iz* and *blk* were calculated in the same way as in CaRU.

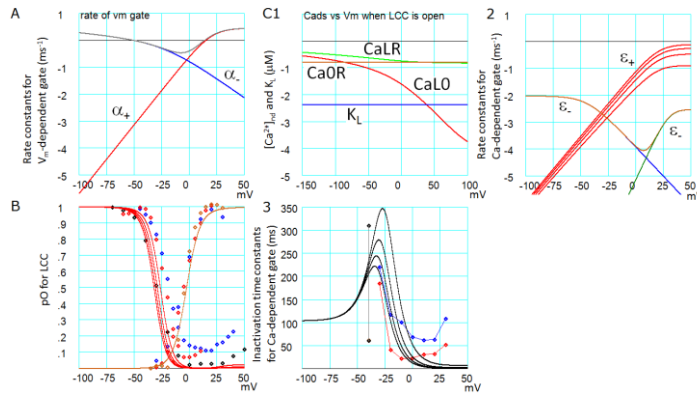


Fig. S2. Determination of LCC gating from the experimental data

A: activation (α_+ , red) and deactivation rate constants (α_- , blue) and the sum of the two rate constants ($1/\tau$, gray). B: the steady-state activation and inactivation of LCC. Data points are from Mewes & Ravens (6) (red), Pelzmann et al. (19) (blue), Magyar et al. (20) (chocolate) and Li et al., (21) (black). C1: the $[Ca^{2+}]_{nd} - V_m$ relations were calculated for Ca_{L0} (red), Ca_{LR} (gray), and Ca_{OR} (chocolate) together with K_L in Eq. S5 (blue). C2: the inactivation rate (at Ca_{L0}) plotted for four $[Ca]_{SRH}$ (ϵ_+ , red curves), and removal rate from inactivation (ϵ_- , chocolate curves) given by the two components in Eq. S6. C3: the V_m -dependence of Ca^{2+} -inactivation τ . Data points are from Beukelmann et al. (1) (red), Pelzmann (19) (blue), Fulop et al., (22) (a single chocolate point) and Pelzmann (19) (black points connected with gray line are the fast and slow components).

$$pO_{LCC_a} = Y_{ooo} + Y_{ooc} \quad (\text{Eq. S7})$$

$$I_{CaL_X_a} = f_{CaL_a} \cdot P_{CaL_X} \cdot GHK_{X_a} \cdot pO_{LCC_a} \cdot \frac{1}{1 + \left(\frac{1.4}{[ATP]}\right)^3} \quad (\text{Eq. S8})$$

a = (blk, iz, jnc), X = (Ca, Na, K). [ATP] was fixed to 6 mM.

Fraction of I_{CaL}

$$f_{CaL_jnc} = 0.75, \quad f_{CaL_bk} = 0.10, \quad f_{CaL_iz} = 0.15$$

Converting factors

$$P_{CaL_Ca} = 14.21$$

$$P_{CaL_Na} = 0.0000185 \cdot P_{CaL_Ca}$$

$$P_{CaL_K} = 0.000367 \cdot P_{CaL_Ca}$$

$$I_{CaL} = (I_{CaL_Ca_jnc} + I_{CaL_Na_jnc} + I_{CaL_K_jnc}) + (I_{CaL_Ca_iz} + I_{CaL_Na_iz} + I_{CaL_K_iz}) + (I_{CaL_Ca_bk} + I_{CaL_Na_bk} + I_{CaL_K_bk}) \quad (\text{Eq. S9})$$

Ca²⁺-mediated inactivation in other models for comparison

Ca^{2+} -mediated inactivation in ORd model was examined under the widely used assumption that the I_{Ba} through LCC was solely due to VDI. This assumption is different from the thorough experimental conclusion by Brunet *et al.* (23) and Ferreira *et al.* (18) (see also Discussion in Grandi *et al.* (24)). Ferreira *et al.* (18) recorded I_{Ba} in the transfected cell-line with the pore-forming $\alpha 1$ subunit in association with β subunits, and revealed that the I_{Ba} decayed as the sum of two exponentials, where the first one ($\tau = 600$ ms at 21 °C) was accompanied with no gating current, but the slow one ($\tau = 6$ s) was with the gating current, indicating that the former is CDI and the latter is VDI. Brunet *et al.* (23) suggested that the CDI of I_{Ba} is mediated by a low affinity binding of Ba^{2+} to calmodulin as has been suggested in foregoing studies (18, 25, 26), and indicated that unambiguous measurement of VDI requires use of Na^+ or another monovalent cation as charge carrier (for the slow inactivation of I_{Na} via LCC, see Matsuda (27)). In HuVEC model, we simply ignored the relatively slow inactivation of I_{Na} for the sake of simplicity.

The time course of LCC inactivation during AP was conventionally examined by recording compensation currents (I_{cp}) during the I_{CaL} blockage in the AP clamp experiment. However, our simulation of the AP clamp indicated (not shown) that I_{cp} is not equal to I_{CaL} , but represents a sum of

modifications of all current components, such as I_{CaL} , I_{NCX} , I_{Ks} , I_{Cab} , $I_{L(ca)}$ and I_{PMCA} caused by blocking the Ca^{2+} -flux of I_{CaL} .

Sodium current (I_{Na})

The same I_{Na} model as in our previous study (13) was used, except for the amplitude parameters, f_L and P_{Na} . I_{Na} is composed of the two components, I_{NaT} and I_{NaL} .

$$I_{Na} = I_{NaT} + I_{NaL} \quad (\text{Eq. S10})$$

Transient component (I_{NaT})

$$\frac{dp(C)_{NaT}}{dt} = k_{OC} \cdot p(O)_{NaT} + k_{I2C} \cdot p(I_2)_{NaT} + k_{Isb} \cdot p(I_s)_{NaT} - (k_{Isf} - f_{C_Na} \cdot (k_{C2O} + k_{C2I2})) \cdot p(C)_{NaT} \quad (\text{Eq. S11})$$

$$\frac{dp(O)_{NaT}}{dt} = k_{I2O} \cdot p(I_2)_{NaT} + f_{C_Na} \cdot k_{C2O} \cdot p(C)_{NaT} - (k_{OC} + k_{OI2}) \cdot p(O)_{NaT} \quad (\text{Eq. S12})$$

$$\frac{dp(I_2)_{NaT}}{dt} = f_{C_Na} \cdot k_{C2I2} \cdot p(C)_{NaT} + k_{OI2} \cdot p(O)_{NaT} + k_{Isb} \cdot p(I_s)_{NaT} - (k_{I2C} + k_{I2O} + k_{Isf}) \cdot p(I_2)_{NaT} \quad (\text{Eq. S13})$$

$$\frac{dp(I_s)_{NaT}}{dt} = k_{Isf} \cdot p(I_2)_{NaT} + k_{Isf} \cdot p(C)_{NaT} - 2 \cdot k_{Isb} \cdot p(I_s)_{NaT} \quad (\text{Eq. S14})$$

$$f_{C_Na} = \frac{C_2}{(C_1 + C_2)} = \frac{1}{1 + \exp\left(-\frac{V_m + 48}{7}\right)} \quad (\text{Eq. S15})$$

$$k_{C2O} = \frac{1}{0.0025 \cdot \exp\left(\frac{V_m}{-8.0}\right) + 0.15 \cdot \exp\left(\frac{V_m}{-100.0}\right)} \quad (\text{Eq. S16})$$

$$k_{OC} = \frac{1}{30.0 \cdot \exp\left(\frac{V_m}{12.0}\right) + 0.53 \cdot \exp\left(\frac{V_m}{50.0}\right)} \quad (\text{Eq. S17})$$

$$k_{OI2} = \frac{1}{0.0433 \cdot \exp\left(\frac{V_m}{-27.0}\right) + 0.34 \cdot \exp\left(\frac{V_m}{-2000.0}\right)} \quad (\text{Eq. S18})$$

$$k_{I2O} = 0.0001312$$

$$k_{C2I2} = \frac{0.5}{1.0 + \frac{k_{I2O} \cdot k_{OC}}{k_{OI2} \cdot k_{C2O}}} \quad (\text{Eq. S19})$$

$$k_{I2C} = 0.5 - k_{C2I2} \quad (\text{Eq. S20})$$

$$k_{Isb} = \frac{1}{300000.0 \cdot \exp\left(\frac{V_m}{10.0}\right) + 50000.0 \cdot \exp\left(\frac{V_m}{16.0}\right)} \quad (\text{Eq. S21})$$

$$k_{Isf} = \frac{1}{0.016 \cdot \exp\left(\frac{V_m}{-9.9}\right) + 8.0 \cdot \exp\left(\frac{V_m}{-45.0}\right)} \quad (\text{Eq. S22})$$

$$I_{NaT} = (1 - f_L) \cdot P_{Na} \cdot (\text{GHK}_{Na} + 0.1 \cdot \text{GHK}_K) \cdot p(O)_{NaT} \quad (\text{Eq. S23})$$

Late component (I_{NaL})

The k_{II2} , k_{OI1} , k_{IO} , k_{IC} and k_{C2I1} are specific for I_{NaL} , and other rate constants are the same as in I_{NaL} .

$$\frac{dp(C)_{NaL}}{dt} = k_{OC} \cdot p(O)_{NaL} + k_{I1C} \cdot p(I_1)_{NaL} + k_{I2C} \cdot p(I_2)_{NaL} + k_{Isb} \cdot p(I_s)_{NaL} - (k_{Isf} + f_{C_Na} \cdot (k_{C2O} + k_{C2I2} + k_{C2I1})) \cdot p(C)_{NaL} \quad (\text{Eq. S24})$$

$$\frac{dp(O)_{NaL}}{dt} = k_{IO} \cdot p(I_1)_{NaL} + f_{C_Na} \cdot k_{C2O} \cdot p(C)_{NaL} - (k_{OC} + k_{OI1}) \cdot p(O)_{NaL} \quad (\text{Eq. S25})$$

$$\frac{dp(I_1)_{NaL}}{dt} = k_{OI1} \cdot p(O)_{NaL} + f_{C_Na} \cdot k_{C2I1} \cdot p(C)_{NaL} - (k_{IO} + k_{IC} + k_{II2}) \cdot p(I_1)_{NaL} \quad (\text{Eq. S26})$$

$$\frac{dp(I_2)_{NaL}}{dt} = f_{C_Na} \cdot k_{C2I2} \cdot p(C)_{NaL} + k_{II2} \cdot p(I_1)_{NaL} + k_{Isb} \cdot p(I_s)_{NaL} - (k_{I2C} + k_{Isf}) \cdot p(I_2)_{NaL} \quad (\text{Eq. S27})$$

$$\frac{dp(I_s)_{NaL}}{dt} = k_{Isf} \cdot p(I_2)_{NaL} + k_{Isf} \cdot p(C)_{NaL} - 2 \cdot k_{Isb} \cdot p(I_s)_{NaL} \quad (\text{Eq. S28})$$

$$k_{II2} = 0.00534$$

$$k_{OI1} = k_{OI2}$$

$$k_{IO} = 0.01$$

$$k_{IC} = k_{I2C}$$

$$k_{C2I1} = k_{C2I2}$$

$$I_{NaL} = f_L \cdot P_{Na} \cdot (GHK_{Na} + 0.1 \cdot GHK_K) \cdot p(O)_{NaL} \quad (\text{Eq. S29})$$

$$f_L = 0.13125, P_{Na} = 8.1072 \quad (\text{pA/mM})$$

Inward rectifier potassium current (I_{K1})

The characteristic inward-going rectification of I_{K1} has been widely observed in mammalian ventricular cells, including human cells. Yan and Ishihara (28) and Ishihara and Yan (29) conducted detailed analysis using transfected 293T cell line and demonstrated the time-dependent kinetic changes in I_{K1} (I_{K1} transient) on repolarization to -30~-50 mV, and explained it by the time lag between the instantaneous relief of Mg^{2+} -block and the relatively slow spermine-block during AP repolarization. We adopted this model after adjusting the amplitude of I_{K1} to obtain a maximum repolarizing rate of ~1 V/s.

$[Mg^{2+}]_{cyt}$ fixed at 0.8 mM for the Mg^{2+} -block in the mode 1, and spermine concentration $[SPM] = 5 \mu\text{M}$.

$$\alpha_{Mg} = 12.0 \cdot \exp(-0.025 \cdot (V_m - E_K)) \quad (\text{Eq. S30})$$

$$\beta_{Mg} = 28 \cdot [Mg^{2+}]_{cyt} \cdot \exp(0.025 \cdot (V_m - E_K)) \quad (\text{Eq. S31})$$

$$f_O = \frac{\alpha_{Mg}}{\alpha_{Mg} + \beta_{Mg}} \quad (\text{Eq. S32})$$

$$f_B = \frac{\beta_{Mg}}{\alpha_{Mg} + \beta_{Mg}} \quad (\text{Eq. S33})$$

$$pO_{Mg} = f_O \cdot f_O \cdot f_O \quad (\text{Eq. S34})$$

$$pO_{Mg1} = 3.0 \cdot f_O \cdot f_O \cdot f_B \quad (\text{Eq. S35})$$

$$pO_{Mg2} = 3.0 \cdot f_O \cdot f_B \cdot f_B \quad (\text{Eq. S36})$$

The SPM-block in the mode 2

$$\alpha_{SPM} = \frac{0.17 \cdot \exp(-0.07 \cdot ((V_m - E_K) + 8 \cdot [Mg^{2+}]_{cyt}))}{1.0 + 0.01 \cdot \exp(0.12 \cdot ((V_m - E_K) + 8 \cdot [Mg^{2+}]_{cyt}))} \quad (\text{Eq. S37})$$

$$\beta_{SPM} = \frac{0.28 \cdot [SPM] \cdot \exp(0.15 \cdot ((V_m - E_K) + 8 \cdot [Mg^{2+}]_{cyt}))}{1.0 + 0.01 \cdot \exp(0.13 \cdot ((V_m - E_K) + 8 \cdot [Mg^{2+}]_{cyt}))} \quad (\text{Eq. S38})$$

$$\frac{dPb_{spm}}{dt} = \beta_{SPM} \cdot pO_{Mg} \cdot (1 - Pb_{spm}) - \alpha_{SPM} \cdot Pb_{spm} \quad (\text{Eq. S39})$$

$$pO_{mode 1} = f_{mode 1} \cdot (1 - Pb_{spm}) \cdot \left(pO_{Mg} + \frac{2}{3} \cdot pO_{Mg1} + \frac{1}{3} \cdot pO_{Mg2} \right) \quad (\text{Eq. S40})$$

$$f_{mode 1} = 0.9$$

$$pO_{mode 2} = \frac{(1 - f_{mode 1})}{1.0 + \frac{[SPM]}{40.0 \cdot \exp\left(\frac{-V_m - E_K}{9.1}\right)}} \quad (\text{Eq. S41})$$

$$p(O)_{K1} = pO_{mode 1} + pO_{mode 2} \quad (\text{Eq. S42})$$

$$\chi_{K1} = \frac{\left(\frac{[K^+]_o}{4.5}\right)^{0.4}}{1.0 + \exp\left(\frac{-[K^+]_o - 2.2}{0.6}\right)} \quad (\text{Eq. S43})$$

$$I_{K1} = G_{K1} \cdot \chi_{K1} \cdot (V_m - E_K) \cdot p(O)_{K1} \quad (\text{Eq. S44})$$

$$G_{K1} = 1.353$$

Delayed rectifier K⁺ current, fast component (I_{Kr})

Different models of I_{Kr} were used in the GPB and ORd models. We adopted the ORd I_{Kr} model, which was developed by referring to the slow inactivation kinetics of I_{Kr} demonstrated in Jost *et al.* (8) and Jost *et al.* (4). We adjusted the amplitude of I_{Kr} to a medium size of I_{Kr} tail currents at -40 or -30 mV among different references (0.25 in Jost *et al.* (8); 0.29 in Jost *et al.* (30), 0.57 in Jost *et al.* (4), 0.31 in Magyar *et al.* (20), 0.32 in Li *et al.* (7), and 0.25 pA/pF in Rajamani *et al.* (31)). The experimental prolongation of APD₉₀ was well reconstructed by blocking I_{Kr} (with a limiting amplitude of ~0.3 pA/pF), which is less than a half of that in ORd model of 0.85 pA/pF (see Results, Fig. 3A1 red and 4 blue).

$$X_{r,\infty} = \frac{1}{1 + \exp\left(\frac{-(V_m + 8.337)}{6.789}\right)} \quad (\text{Eq. S45})$$

$$\tau_{Xr,fast} = 12.98 + \frac{1}{0.3652 \cdot \exp\left(\frac{V_m - 31.66}{3.869}\right) + 4.123 \cdot 10^{-5} \cdot \exp\left(\frac{-(V_m - 47.78)}{20.38}\right)} \quad (\text{Eq. S46})$$

$$\tau_{Xr,slow} = 1.865 + \frac{1}{0.06629 \cdot \exp\left(\frac{V_m - 34.70}{7.355}\right) + 1.128 \cdot 10^{-5} \cdot \exp\left(\frac{-(V_m - 29.74)}{25.94}\right)} \quad (\text{Eq. S47})$$

$$A_{Xr,fast} = \frac{1}{1 + \exp\left(\frac{V_m + 4.81}{38.21}\right)} \quad (\text{Eq. S48})$$

$$A_{Xr,slow} = 1 - A_{Xr,fast} \quad (\text{Eq. S49})$$

$$\frac{dX_{r,fast}}{dt} = \frac{X_{r,\infty} - X_{r,fast}}{\tau_{Xr,fast}} \quad (\text{Eq. S50})$$

$$\frac{dX_{r,slow}}{dt} = \frac{X_{r,\infty} - X_{r,slow}}{\tau_{Xr,slow}} \quad (\text{Eq. S51})$$

$$X_r = A_{Xr,fast} \cdot X_{r,fast} + A_{Xr,slow} \cdot X_{r,slow} \quad (\text{Eq. S52})$$

$$R_{Kr} = \frac{1}{\left(1 + \exp\left(\frac{V_m + 55}{75}\right)\right) \cdot \left(1 + \exp\left(\frac{V_m - 10}{30}\right)\right)} \quad (\text{Eq. S53})$$

$$p(O)_{Kr} = X_r \cdot R_{Kr} \quad (\text{Eq. S54})$$

$$\chi_{Kr} = \sqrt{\frac{[K^+]_o}{4.5}} \quad (\text{Eq. S55})$$

$$I_{Kr} = G_{Kr} \cdot \chi_{Kr} \cdot (V_m - E_K) \cdot p(O)_{Kr} \quad (\text{Eq. S56})$$

$$G_{Kr} = 0.0166$$

Delayed rectifier K⁺ current, slow component (I_{Ks})

The gating kinetics of ORd model was used after separating I_{Ks} into two components, I_{Ks_K} and I_{Ks_Na} and using the GHK equation. The permeability ratio, P_{Na} : P_K = 0.04 : 1.

$$para_{Xs1_a,\infty} = \frac{1}{1 + \exp\left(\frac{-(V_m + 11.60)}{8.932}\right)} \quad (\text{Eq. S57})$$

$$\tau_{Xs1_a} = 817.3 + \frac{1}{2.326 \cdot 10^{-4} \cdot \exp\left(\frac{V_m + 48.28}{17.80}\right) + 0.001292 \cdot \exp\left(\frac{-(V_m + 210.0)}{230.0}\right)} \quad (\text{Eq. S58})$$

$$\frac{dpara_{Xs1_a}}{dt} = \frac{para_{Xs1_a,\infty} - para_{Xs1_a}}{\tau_{Xs1_a}} \quad (\text{Eq. S59})$$

$$para_{Xs2_a,\infty} = para_{Xs1_a,\infty} \quad (\text{Eq. S60})$$

$$\tau_{Xs2_a} = \frac{1}{0.01 \cdot \exp\left(\frac{V_m - 50}{20}\right) + 0.0193 \cdot \exp\left(\frac{-(V_m + 66.54)}{31}\right)} \quad (\text{Eq. S61})$$

$$\frac{dpara_{Xs2_a}}{dt} = \frac{para_{Xs2_a,\infty} - para_{Xs2_a}}{\tau_{Xs2_a}} \quad (\text{Eq. S62})$$

$$para_{Rks_a} = 1 + \frac{0.6}{1 + \left(\frac{0.000038}{[Ca^{2+}]_a}\right)^{1.4}} \quad (\text{Eq. S63})$$

$$p(O)_{Ks_a} = para_{Xs1_a} \cdot para_{Xs2_a} \cdot para_{Rks_a} \quad (\text{Eq. S64})$$

$$I_{Ks_X_a} = f_{Ks_a} \cdot P_{Ks_X} \cdot GHK_X \cdot p(O)_{Ks_a} \quad (\text{Eq. S65})$$

a = (blk, iz), X = (K, Na)

$$f_{Ks_iz} = 0.1, f_{Ks_blk} = 0.9$$

Converting factors

$$P_{Ks_K} = 0.002782, P_{Ks_Na} = 0.04 \cdot P_{Ks_K}$$

$$I_{Ks} = (I_{Ks_K_iz} + I_{Ks_Na_iz}) + (I_{Ks_K_blk} + I_{Ks_Na_blk}) \quad (\text{Eq. S66})$$

Transient outward K⁺ current (I_{Kto})

The gating kinetics of the ORd model was used after adjusting G_{Kto}.

$$a_{\infty} = \frac{1}{1 + \exp\left(\frac{-(V_m - 14.34)}{14.82}\right)} \quad (\text{Eq. S67})$$

$$\tau_a = \frac{1.0515}{\frac{1}{1.2089 \left(1 + \exp\left(\frac{-(V_m - 18.41)}{29.38}\right)\right)} + \frac{3.5}{1 + \exp\left(\frac{V_m + 100}{29.38}\right)}} \quad (\text{Eq. S68})$$

$$\frac{da}{dt} = \frac{a_{\infty} - a}{\tau_a} \quad (\text{Eq. S69})$$

$$i_{\infty} = \frac{1}{1 + \exp\left(\frac{V_m + 43.94}{5.711}\right)} \quad (\text{Eq. S70})$$

$$\tau_{i,fast} = 4.562 + \frac{1}{0.3933 \cdot \exp\left(\frac{-(V_m + 100)}{100}\right) + 0.08004 \cdot \exp\left(\frac{V_m + 50}{16.59}\right)} \quad (\text{Eq. S71})$$

$$\tau_{i,slow} = 23.62 + \frac{1}{0.001416 \cdot \exp\left(\frac{-(V_m + 96.52)}{59.05}\right) + 1.7808 \cdot 10^{-8} \cdot \exp\left(\frac{V_m + 114.1}{8.079}\right)} \quad (\text{Eq. S72})$$

$$A_{i,fast} = \frac{1}{1 + \exp\left(\frac{V_m - 213.6}{151.2}\right)} \quad (\text{Eq. S73})$$

$$A_{i,slow} = 1 - A_{i,fast} \quad (\text{Eq. S74})$$

$$\frac{di_{fast}}{dt} = \frac{i_{\infty} - i_{fast}}{\tau_{i,fast}} \quad (\text{Eq. S75})$$

$$\frac{di_{slow}}{dt} = \frac{i_{\infty} - i_{slow}}{\tau_{i,slow}} \quad (\text{Eq. S76})$$

$$i = A_{i,fast} \cdot i_{fast} + A_{i,slow} \cdot i_{slow} \quad (\text{Eq. S77})$$

$$p(O)_{Kto} = a \cdot i \quad (\text{Eq. S78})$$

$$I_{Kto} = G_{Kto} \cdot p(O)_{Kto} \cdot (V_m - E_K) \quad (\text{Eq. S79})$$

$$G_{Kto} = 0.0312$$

Time-independent currents

All these currents are from Takeuchi *et al.* (32) as described in Asakura *et al.* (13).

Voltage-dependent potassium current (plateau current) (I_{Kpl})

$$p(O)_{Kpl} = \frac{V_m}{1 - \exp\left(\frac{-V_m}{13.0}\right)} \quad (\text{Eq. S80})$$

$$\chi_{Kpl} = \left(\frac{[K^+]_o}{5.4}\right)^{0.16} \quad (\text{Eq. S81})$$

$$I_{Kpl} = P_{Kpl} \cdot \chi_{Kpl} \cdot p(O)_{Kpl} \cdot GHK_K \quad (\text{Eq. S82})$$

$$P_{Kpl} = 0.0000172$$

Background calcium current (I_{Cab})

$$I_{Cab_a} = P_{Cab_a} \cdot f_{Cab_a} \cdot GHK_{Ca}, \quad a = (\text{blk}, \text{iz}) \quad (\text{Eq. S83})$$

$$P_{Cab_a} = 0.00006822$$

Fraction of I_{Cab}

$$f_{Cab_{iz}} = 0.1, \quad f_{Cab_{blk}} = 0.9$$

$$I_{Cab} = I_{Cab_{iz}} + I_{Cab_{blk}} \quad (\text{Eq. S84})$$

Background non-selective cation current (I_{bNSC})

$$I_{bNSC_X} = P_{bNSC_X} \cdot GHK_X, \quad X = (K, Na) \quad (\text{Eq. S85})$$

$$P_{bNSC_K} = 0.00014, \quad P_{bNSC_Na} = 0.00035$$

$$I_{bNSC} = I_{bNSC_K} + I_{bNSC_Na} \quad (\text{Eq. S86})$$

Calcium-activated background cation current ($I_{I(Ca)}$)

$$p(O)_a = \frac{1.0}{1.0 + \left(\frac{0.0012}{[Ca^{2+}]_a} \right)^3} \quad (\text{Eq. S87})$$

$$I_{I(Ca)_X_a} = P_{I(Ca)_X} \cdot f_{I(Ca)_a} \cdot GHK_X \cdot p(O)_a \quad X = (Na, K), \quad a = (blk, iz) \quad (\text{Eq. S88})$$

$$P_{I(Ca)_Na} = 0.00273$$

$$P_{I(Ca)_K} = P_{I(Ca)_Na}$$

Fraction of $I_{I(Ca)}$

$$f_{I(Ca)_iz} = 0.1, \quad f_{I(Ca)_blk} = 0.9$$

$$I_{I(Ca)} = I_{I(Ca)_Na_iz} + I_{I(Ca)_K_iz} + I_{I(Ca)_Na_blk} + I_{I(Ca)_K_blk} \quad (\text{Eq. S89})$$

ATP-sensitive potassium current (I_{KATP})

$$p(O)_{KATP} = \frac{0.8}{1.0 + \left(\frac{[ATP]_{kyl}}{0.1} \right)^2} \quad (\text{Eq. S90})$$

$$\chi_{KATP} = 0.0236 \cdot ([K^+]_o)^{0.24} \quad (\text{Eq. S91})$$

$$I_{KATP} = G_{KATP} \cdot (V_m - E_K) \cdot p(O)_{KATP} \cdot \chi_{KATP} \quad (\text{Eq. S92})$$

$$G_{KATP} = 17.674$$

Na⁺/K⁺ pump current (I_{NaK})

As described in PBMB, the Na⁺/K⁺ pump model developed by Oka *et al.* (33) on the framework of Smith and Crampin (34) was used after adjusting Amp_{NaK}.

$$\overline{Na}_i = \frac{[Na^+]_i}{K_{d,Na_i}} \quad (\text{Eq. S93})$$

$$\overline{Na}_o = \frac{[Na^+]_o}{K_{d,Na_o}} \quad (\text{Eq. S94})$$

$$\overline{K}_i = \frac{[K^+]_i}{K_{d,K_i}} \quad (\text{Eq. S95})$$

$$\overline{K}_o = \frac{[K^+]_o}{K_{d,K_o}} \quad (\text{Eq. S96})$$

$$\overline{\text{MgATP}} = \frac{[\text{MgATP}]_{\text{cyl}}}{K_{d,\text{MgATP}}} \quad (\text{Eq. S97})$$

$$K_{d,\text{Na}o} = K_{d,\text{Na}o}^0 \cdot \exp \frac{\Delta_{\text{Na}o} \cdot FV_m}{RT} \quad (\text{Eq. S98})$$

$$K_{d,\text{Na}i} = K_{d,\text{Na}i}^0 \cdot \exp \frac{\Delta_{\text{Na}i} \cdot FV_m}{RT} \quad (\text{Eq. S99})$$

$$K_{d,\text{K}o} = K_{d,\text{K}o}^0 \cdot \exp \frac{\Delta_{\text{K}o} \cdot FV_m}{RT} \quad (\text{Eq. S100})$$

$$K_{d,\text{K}i} = K_{d,\text{K}i}^0 \cdot \exp \frac{\Delta_{\text{K}i} \cdot FV_m}{RT} \quad (\text{Eq. S101})$$

$$K_{d,\text{Na}i}^0 = 5, \quad K_{d,\text{Na}e}^0 = 26.8, \quad K_{d,\text{K}i}^0 = 18.8, \quad K_{d,\text{K}e}^0 = 0.8, \quad K_{d,\text{MgATP}} = 0.6$$

$$\Delta_{\text{Na}i} = -0.14, \quad \Delta_{\text{Na}o} = 0.44, \quad \Delta_{\text{K}i} = -0.14, \quad \Delta_{\text{K}o} = 0.23$$

$$\alpha_1^+ = \frac{k_1^+ \overline{\text{Na}_i}^3}{(1 + \overline{\text{Na}_i})^3 + (1 + \overline{\text{K}_i})^2 - 1} \quad (\text{Eq. S102})$$

$$\alpha_2^+ = k_2^+ \quad (\text{Eq. S103})$$

$$\alpha_3^+ = \frac{k_3^+ \overline{\text{K}_o}^2}{(1 + \overline{\text{Na}_o})^3 + (1 + \overline{\text{K}_o})^2 - 1} \quad (\text{Eq. S104})$$

$$\alpha_4^+ = \frac{k_4^+ \overline{\text{MgATP}}}{1 + \overline{\text{MgATP}}} \quad (\text{Eq. S105})$$

$$\alpha_1^- = k_1^- [\text{MgADP}]_{\text{cyl}} \quad (\text{Eq. S106})$$

$$\alpha_2^- = \frac{k_2^- \overline{\text{Na}_o}^3}{(1 + \overline{\text{Na}_o})^3 + (1 + \overline{\text{K}_o})^2 - 1} \quad (\text{Eq. S107})$$

$$\alpha_3^- = \frac{k_3^- [\text{Pi}][\text{H}^+]}{1 + \overline{\text{MgATP}}} \quad (\text{Eq. S108})$$

$$\alpha_4^- = \frac{k_4^- \overline{\text{K}_i}^2}{(1 + \overline{\text{Na}_i})^3 + (1 + \overline{\text{K}_i})^2 - 1} \quad (\text{Eq. S109})$$

$$k_1^+ = 0.72, \quad k_1^- = 0.08, \quad k_2^+ = 0.08, \quad k_2^- = 0.008, \quad k_3^+ = 4, \quad k_3^- = 8000, \quad k_4^+ = 0.3, \quad k_4^- = 0.2 \quad (\text{Eq. S110})$$

$$\frac{dP_7}{dt} = -\alpha_2^+ \cdot P_7 + \alpha_2^- \cdot P_{8,13} + \alpha_1^+ \cdot P_{1,6} - \alpha_1^- \cdot P_7 \quad (\text{Eq. S111})$$

$$\frac{dP_{8,13}}{dt} = -\alpha_3^+ \cdot P_{8,13} + \alpha_3^- \cdot P_{14,15} + \alpha_2^+ \cdot P_7 - \alpha_2^- \cdot P_{8,13} \quad (\text{Eq. S112})$$

$$V_{\text{step1}} = \alpha_1^+ \cdot P_{1,6} - \alpha_1^- \cdot P_7 \quad (\text{Eq. S113})$$

$$V_{\text{step2}} = \alpha_2^+ \cdot P_7 - \alpha_2^- \cdot P_{8,13} \quad (\text{Eq. S114})$$

$$V_{\text{step3}} = \alpha_3^+ \cdot P_{8,13} - \alpha_3^- \cdot P_{14,15} \quad (\text{Eq. S115})$$

$$V_{step4} = \alpha_4^+ \cdot P_{14,15} - \alpha_4^- \cdot P_{1,6} \quad (\text{Eq. S116})$$

$$v_{cyc_NaK} = V_{step2} \quad (\text{Eq. S117})$$

$$I_{NaK} = Amp_{NaK} \cdot v_{cyc_NaK} \quad (\text{Eq. S118})$$

$$Amp_{NaK} = 25.178 \quad (\text{Eq. S119})$$

$$I_{NaK_Na} = Stoi_{NaK_Na} \cdot I_{NaK} \quad Stoi_{NaK_Na} = 3, \quad I_{NaK_K} = Stoi_{NaK_K} \cdot I_{NaK} \quad (\text{Eq. S119})$$

$$Stoi_{NaK_K} = -2 \quad (\text{Eq. S120})$$

Na⁺/Ca²⁺ exchange current (INCX)

The NCX model developed by Takeuchi *et al.* (32) was used after adjusting the amplitude factor

Amp_{NCX}.

a = (blk, iz)

$$\alpha_{1_a} = q_a(E_1Na) \cdot (f_{Caina_a} \cdot \alpha_{1_on} + (1 - f_{Caina_a}) \cdot \alpha_{1_off}) \quad (\text{Eq. S121})$$

$$\beta_{1_a} = f_{Caina_a} \cdot \beta_{1_on} + (1 - f_{Caina_a}) \cdot \beta_{1_off} \quad (\text{Eq. S122})$$

$$\alpha_{2_a} = f_{Caina_a} \cdot \alpha_{2_on} + (1 - f_{Caina_a}) \cdot \alpha_{2_off} \quad (\text{Eq. S123})$$

$$\beta_{2_a} = f_{Caina_a} \cdot \beta_{2_on} + (1 - f_{Caina_a}) \cdot \beta_{2_off} \quad (\text{Eq. S124})$$

$$\alpha_{1_on} = 0.002, \quad \alpha_{1_off} = 0.0015, \quad \beta_{1_on} = 0.0012, \quad \beta_{1_off} = 0.0000005$$

$$\alpha_{2_on} = 0.000006, \quad \alpha_{2_off} = 0.02, \quad \beta_{2_on} = 0.18, \quad \beta_{2_off} = 0.0002$$

$$\alpha_E = k_2 \cdot q(E_2Na) + k_4 \cdot q(E_2Ca) \quad (\text{Eq. S125})$$

$$\beta_{E_a} = k_1 \cdot q_a(E_1Na) + k_3 \cdot q_a(E_1Ca) \quad (\text{Eq. S126})$$

$$k_1 = \exp\left(\frac{0.32 \cdot F \cdot V_m}{R \cdot T}\right) \quad (\text{Eq. S127})$$

$$k_2 = \exp\left(\frac{(0.32 - 1) \cdot F \cdot V_m}{R \cdot T}\right) \quad (\text{Eq. S128})$$

$$k_3 = 1.0, \quad k_4 = 1.0$$

$$f_{Caina_a} = \frac{[Ca^{2+}]_a}{[Ca^{2+}]_a + K_{m,act}} \quad (\text{Eq. S129})$$

$$K_{m,act} = 0.004$$

$$\frac{dp(E_1)_{NCX_a}}{dt} = p(E_2)_{NCX_a} \cdot \alpha_E + p(I_1)_{NCX_a} \cdot \beta_{1_a} + p(I_2)_{NCX_a} \cdot \beta_{2_a} - p(E_1)_{NCX_a} \cdot (\beta_{E_a} + \alpha_{1_X} + \alpha_{2_X})$$

(Eq. S130)

$$\frac{dp(I_1)_{NCX_a}}{dt} = p(E_1)_{NCX_a} \cdot \alpha_{1_a} - p(I_1)_{NCX_a} \cdot \beta_{1_a}$$

(Eq. S131)

$$\frac{dp(I_2)_{NCX_a}}{dt} = p(E_1)_{NCX_a} \cdot \alpha_{2_a} - p(I_2)_{NCX_a} \cdot \beta_{2_a}$$

(Eq. S132)

$$p(E_2)_{NCX_a} = 1 - p(E_1)_{NCX_a} - p(I_1)_{NCX_a} - p(I_2)_{NCX_a}$$

(Eq. S133)

$$q_a(E_1Na) = \frac{1.0}{\left(1.0 + \left(\frac{K_{m,Nai}}{[Na^+]_i}\right)^3\right) \cdot \left(1.0 + \frac{[Ca^{2+}]_a}{K_{m,Cai}}\right)}$$

(Eq. S134)

$$q_a(E_1Ca) = \frac{1.0}{\left(1.0 + \frac{K_{m,Cai}}{[Ca^{2+}]_a}\right) \cdot \left(1.0 + \left(\frac{[Na^+]_i}{K_{m,Nai}}\right)^3\right)}$$

(Eq. S135)

$$q(E_2Na) = \frac{1.0}{\left(1.0 + \left(\frac{K_{m,Nao}}{[Na^+]_o}\right)^3\right) \cdot \left(1.0 + \frac{[Ca^{2+}]_o}{K_{m,Cao}}\right)}$$

(Eq. S136)

$$q(E_2Ca) = \frac{1.0}{\left(1.0 + \frac{K_{m,Cao}}{[Ca^{2+}]_o}\right) \cdot \left(1.0 + \left(\frac{[Na^+]_o}{K_{m,Nao}}\right)^3\right)}$$

(Eq. S137)

$$K_{m,Nao} = 87.5, \quad K_{m,Nai} = 20.74854, \quad K_{m,Cao} = 1.38, \quad K_{m,Cai} = 0.0184$$

$$v_{cyc_NCX_a} = k_1 \cdot q_a(E_1Na) \cdot p(E_1)_{NCX_a} - k_2 \cdot q_a(E_2Na) \cdot p(E_2)_{NCX_a}$$

(Eq. S138)

$$I_{NCX_a} = f_{NCX_a} \cdot Amp_{NCX} \cdot v_{cyc_NCX_a}$$

(Eq. S139)

$$Amp_{NCX} = 30.53$$

$$I_{NCX} = I_{NCX_iz} + I_{NCX_blk}$$

(Eq. S140)

$$f_{NCX_iz} = 0.1, \quad f_{NCX_blk} = 0.9$$

$$I_{NCX_Na_a} = 3 \cdot I_{NCX_a}$$

(Eq. S141)

$$I_{NCX_Ca_a} = -2 \cdot I_{NCX_a}$$

(Eq. S142)

Plasma membrane Ca²⁺-ATPase current (I_{PMCA})

The model equation used in Grandi *et al.* (35) was used for spaces *iz* and *blk* after adjusting the amplitude factor Amp_{PMCA} and K_m.

$$I_{PMCA_a} = f_{PMCA_a} \cdot Amp_{PMCA} \cdot \frac{([Ca^{2+}]_a)^{1.6}}{(K_m)^{1.6} + ([Ca^{2+}]_a)^{1.6}} \quad (\text{Eq. S143})$$

a = (blk, iz)

$$f_{PMCA_iz} = 0.1, \quad f_{PMCA_blk} = 0.9, \quad Amp_{PMCA} = 0.19, \quad K_m = 0.0005$$

$$I_{PMCA} = I_{PMCA_iz} + I_{PMCA_blk} \quad (\text{Eq. S144})$$

CaRU

LCC

The tightly coupled LCC-RyR kinetic model developed by Hinch *et al.* (36) was used after modifications. The new LCC model is described in the section L-type Ca²⁺ current.

RyR channel

The state transition of a RyR is defined by the two-state transition with the activation rate, k_{co} and deactivation rate k_{oc} .

$$k_{co} = Q_{10} \cdot \frac{0.4}{1 + \left(\frac{0.025}{[Ca^{2+}]_{nd}}\right)^{2.7}} \quad (\text{Eq. S145})$$

The $[Ca^{2+}]_{nd}$ for the activation is,

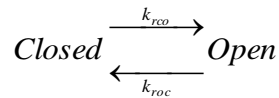
$[Ca^{2+}]_{nd} = Ca_{L0}$ for LCC-dependent activation of a RyR

$[Ca^{2+}]_{nd} = Ca_{00}$ for spontaneous activation of a RyR

$$k_{oc} = Q_{10} \cdot 0.5664 \quad (\text{Eq. S146})$$

$$f_i = \frac{k_{co}}{k_{co} + k_{oc}} \quad (\text{Eq. S147})$$

The state transition of couplon at the regenerative step is also described by the two-state transition scheme.



The activation rate k_{rco} and the deactivation rate k_{roc} are,

$$k_{rco} = f_n \cdot f_i \cdot k_{co} \cdot (sloc0 + [Ca^{2+}]_{SRrl}) \quad (\text{Eq. S148})$$

$$f_n = 7, \quad sloc0 = 0.1$$

$[Ca^{2+}]_{nd} = Ca_{LR}$ for LCC-dependent activation,

$[Ca^{2+}]_{nd} = Ca_{0R}$ for RyR-dependent spontaneous activation,

$$k_{roc} = k_{oc} \cdot pC^{((N_{RyR}-1) \cdot 0.74)} \quad pC = \frac{k_{oc}}{k_{oc} + f_t \cdot \frac{k_{rco}}{f_n}} \quad (\text{Eq. S149})$$

The f_t in Eq. S149 is calculated using Ca_{00} . N_{RyR} is the number of RyRs in a couplon and assumed to be 10.

The $[Ca^{2+}]_{nd}$ (indicated in Fig. 1) is defined as Ca_{00} , Ca_{0R} , Ca_{L0} or Ca_{LR} .

LCC closed; RyR closed:

$$Ca_{00} = [Ca^{2+}]_{jnc} \quad (\text{Eq. S150})$$

LCC closed; RyR open:

$$Ca_{0R} = \frac{Ca_{00} + f_R \cdot [Ca^{2+}]_{SRrI}}{1 + f_R} \quad (\text{Eq. S151})$$

$$f_R = 0.31$$

LCC open; RyR closed:

$$Ca_{L0} = \frac{Ca_{00} + f_L \cdot \frac{\delta V \cdot e^{-\delta V}}{1 - e^{-\delta V}} \cdot [Ca^{2+}]_o}{(1 + f_L \cdot \frac{\delta V}{1 - e^{-\delta V}})} \quad (\text{Eq. S152})$$

$$f_L = 0.014$$

LCC open; RyR open:

$$Ca_{LR} = \frac{Ca_{00} + f_R \cdot [Ca^{2+}]_{SRrI} + f_L \cdot \frac{\delta V \cdot e^{-\delta V}}{1 - e^{-\delta V}} \cdot [Ca^{2+}]_o}{1 + f_R + f_L \cdot \frac{\delta V}{1 - e^{-\delta V}}} \quad (\text{Eq. S153})$$

$$\delta = \frac{2 \cdot F}{R \cdot T} \quad (\text{Eq. S154})$$

$$p(O)_h = p(O) + p(O)_{base} \quad (\text{Eq. S155})$$

$$p(O)_{base} = 0.000075$$

$$p(O) = Y_{ooo} + Y_{coo} + Y_{cco} + Y_{oco} \quad (\text{Eq. S156})$$

$$J_{Ca_rel} = P_{RyR} \cdot p(O)_h \cdot ([Ca^{2+}]_{SRrI} - [Ca^{2+}]_{jnc}) \cdot Sc_cell \quad (\text{Eq. S157})$$

$$P_{RyR} = 5967.67 \quad (\text{fL} \cdot \text{ms}^{-1}) \quad (\text{whole cell})$$

Sarcoplasmic reticulum Ca^{2+} pump (SERCA) current (J_{SERCA})

The three-state model developed by Tran *et al.* (37) was used after several minor modifications as described in Asakura *et al.* (2014) (13). The limiting amplitude of J_{SERCA} , ampSERCA, was

modified.

$$\alpha 1 = 25900 \cdot [\text{MgATP}] \quad (\text{Eq. S158})$$

$$\alpha 2 = \frac{2540}{1 + \left(\frac{Kd_{Cai}}{[Ca^{2+}]_{blk}} \right)^{1.7}} \quad (\text{Eq. S159})$$

$$K_{dCai} = 0.0027 \text{ (mM)}$$

$$\alpha 3 = \frac{5.35}{1 + \left(\frac{[Ca^{2+}]_{SRup}}{Kd_{Casr}} \right)^{1.7}} \quad (\text{Eq. S160})$$

$$K_{dCasr} = 1.378 \text{ (mM)}$$

$$\beta 1 = \frac{0.1972}{1 + \left(\frac{[Ca^{2+}]_{blk}}{Kd_{Cai}} \right)^{1.7}} \quad (\text{Eq. S161})$$

$$\beta 2 = \frac{25435 \cdot [\text{MgADP}]_{\text{cyl}}}{1 + \left(\frac{Kd_{Casr}}{[Ca^{2+}]_{SRup}} \right)^{1.7}} \quad (\text{Eq. S162})$$

$$\beta 3 = 149 \cdot [\text{Pi}] \quad (\text{Eq. S163})$$

$$v_{\text{cyc}} = \frac{6.86 \cdot (\alpha 1 \cdot \alpha 2 \cdot \alpha 3 - \beta 1 \cdot \beta 2 \cdot \beta 3)}{\alpha 2 \cdot \alpha 3 + \beta 1 \cdot \alpha 3 + \beta 1 \cdot \beta 2 + \alpha 1 \cdot \alpha 3 + \beta 2 \cdot \alpha 1 + \beta 2 \cdot \beta 3 + \alpha 1 \cdot \alpha 2 + \beta 3 \cdot \beta 1 + \beta 3 \cdot \alpha 2} \quad (\text{Eq. S164})$$

$$J_{\text{SERCA}} = \frac{\text{ampSERCA} \cdot v_{\text{cyc}}}{2 \cdot F} \cdot Sc_{\text{cell}} \quad (\text{Eq. S165})$$

$$\text{ampSERCA} = 106.4448 \text{ (mmol.ms}^{-1}\text{)}$$

Rate of change in the membrane potential and ion concentrations

Membrane potential

$$\frac{dV_m}{dt} = -(I_{\text{tot_cell}} + I_{\text{app}}) \quad (\text{Eq. S166})$$

$$I_{\text{tot_cell}} = I_{\text{tot_Na}} + I_{\text{tot_Ca}} + I_{\text{tot_K}} \quad (\text{Eq. S167})$$

$$I_{\text{tot_Ca}} = I_{\text{tot_Ca_jnc}} + I_{\text{tot_Ca_iz}} + I_{\text{tot_Ca_blk}} \quad (\text{Eq. S168})$$

$$I_{\text{tot_Ca_jnc}} = I_{\text{CaL_Ca_LR}} + I_{\text{CaL_Ca_L0}} \quad (\text{Eq. S169})$$

$$I_{tot_Ca_iz} = I_{CaL_Ca_iz} + I_{PMCA_iz} + I_{NCX_Ca_iz} + I_{Cab_iz} \quad (\text{Eq. S170})$$

$$I_{tot_Ca_blk} = I_{CaL_Ca_blk} + I_{PMCA_blk} + I_{NCX_Ca_blk} + I_{Cab_blk} \quad (\text{Eq. S171})$$

$$I_{tot_Na} = (I_{CaL_Na_jnc} + I_{CaL_Na_iz} + I_{CaL_Na_blk}) + (I_{NCX_Na_iz} + I_{NCX_Na_blk}) \\ + (I_{Ks_Na_iz} + I_{Ks_Na_blk}) + I_{NaT_Na} + I_{NaL_Na} + I_{NaK_Na} + I_{Kto_Na} + I_{bNSC_Na} + (I_{LCCa_Na_iz} + I_{LCCa_Na_blk}) \quad (\text{Eq. S172})$$

$$I_{tot_K} = (I_{CaL_K_jnc} + I_{CaL_K_iz} + I_{CaL_K_blk}) + I_{NaT_K} + I_{NaL_K} + I_{K1_K} + I_{Kr_K} + (I_{Ks_K_iz} + I_{Ks_K_blk}) \\ + I_{Kto_K} + I_{Kpl} + I_{NaK_K} + I_{KATP_K_cyt} + I_{bNSC_K} + (I_{LCCa_K_iz} + I_{LCCa_K_blk}) \quad (\text{Eq. S173})$$

Ion concentrations

$$\frac{d[Ca^{2+}]_{jnc}}{dt} = -\frac{I_{tot_Ca_jnc} \cdot C_m}{V_{jnc} \cdot 2 \cdot F} + \frac{J_{Ca_rel}}{V_{jnc}} - \frac{J_{Ca_jnciz}}{V_{jnc}} \quad (\text{Eq. S174})$$

$$\frac{d[Ca^{2+}]_{iz}}{dt} = -\frac{I_{tot_Ca_iz} \cdot C_m}{V_{iz} \cdot 2 \cdot F} + \frac{J_{Ca_jnciz}}{V_{iz}} - \frac{J_{Ca_izblk}}{V_{iz}} \quad (\text{Eq. S175})$$

$$\frac{d[Ca^{2+}]_{blk}}{dt} = -\frac{I_{tot_Ca_blk} \cdot C_m}{V_{blk} \cdot 2 \cdot F} - \frac{J_{Ca_SERCA}}{V_{blk}} + \frac{J_{Ca_izblk}}{V_{blk}} \quad (\text{Eq. S176})$$

$$\frac{d[Ca^{2+}]_{SRup}}{dt} = \frac{J_{SERCA}}{V_{SRup}} - \frac{J_{trans_SR}}{V_{SRup}} \quad (\text{Eq. S177})$$

$$\frac{d[Ca^{2+}]_{SRrl}}{dt} = \frac{J_{trans_SR}}{V_{SRrl}} - \frac{J_{rel_SR}}{V_{SRrl}} \quad (\text{Eq. S178})$$

$$\frac{d[Na^+]_i}{dt} = -\frac{I_{tot_Na} \cdot C_m}{V_{cyt} \cdot F} \quad (\text{Eq. S179})$$

$$\frac{d[K^+]_i}{dt} = -\frac{(I_{tot_K} + I_{app}) \cdot C_m}{V_{cyt} \cdot F} \quad (\text{Eq. S180})$$

Contraction

The original model of Negroni and Lascano (38) was used. The magnitude of Fb is given in a unit of mN mm⁻². The binding of Ca²⁺ to a troponin system (TS) having 3 Ca²⁺ binding sites (given in μM) was included in the equation of determining the concentration of free Ca²⁺ in the bulk compartment.

$$[Ca^{2+}]_{blk} = [Ca_{total}]_{blk} - (CaMCA + TnChCa + SRCa + \frac{3 \cdot (TSCa_3 + TSCa_3^{\sim} + TSCa_3^*)}{1000}) \quad (\text{Eq. S181})$$

Supplemental Figures and Tables

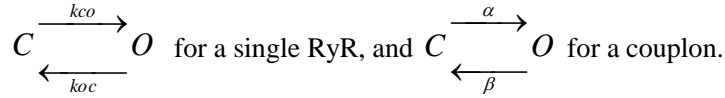
Determination of the deactivation rate of a couplon

Determination of the closing rate (Eq. S149) of the Hinch-type couplon model

The closing rate of a couplon may be different from that of single RyR. We addressed this question by comparing the closing rate between a single RyR and a regenerative couplon by examining the statistical distribution of open times, which is described by a monoexponential decay function of the form:

$$f(t) = N_e \cdot e^{-\frac{t}{\tau}} \quad (\text{Eq. S182})$$

where $f(t)$ is the number of observed open events of life time t , N_e is the total number of open events, and τ is the inverse of the transition rate. The two-state transition schemes defined for both RyR and couplon in the present study are,



In the following analysis, 10 RyRs ($N_{\text{RyR}} = 10$), which have no co-operativity, were assumed in a single couplon. For simplicity, the couplon closed state was defined as the state when all RyRs were closed, and the open state when one or more RyRs were open at any given time.

The effects of the multiple openings of RyRs within a couplon on the closing rate

Using the transition rates, k_{close} and k_{open} , in the LC model, we calculated the stochastic state transitions of individual RyRs within the couplon and Fig. S3A shows a sample segment of reconstructed time course of state transitions of RyRs. The couplon close times (t_c) are indicated by the thick black bars under the record, and thus the open time (t_o) is indicated by the interval between two sequential black bars. The distribution of t_o was analysed by constructing histograms of number of observation in panel B. An attempt to fit a single exponential using single RyR kinetics (k_{oc}) (Eq. S183) to the histogram (red curve in panel B) was clearly unsatisfactory. The distribution of $f(t_o)$ of a couplon showed a marked deviation from a single exponential at longer t_o events.

$$f(t_o) = N_e \cdot e^{-k_{oc} \cdot t_o} \quad (\text{Eq. S183})$$

We assumed that this deviation resulted from multiple open events (MOEs) overlapping with single level opening, which are shown by green bars ($t_{m,i}$) in Fig. S3A. To test this view, we subtracted the sum of $t_{m,i}$ from t_o (Eq. S184) to define a corrected open time (t_o') as in Eq. S184.

$$t_o' = t_o - \sum_{i=1}^k t_{m,i} \quad (\text{Eq. S184})$$

The red line in Fig. S3B fitted well to the $f(t_o')$ (Eq. S185) in Fig. S3C, suggesting that MOEs are indeed responsible for the deviation of the couplon open dwell time histograms in Fig. S3B from a monoexponential function calculated using single RyR kinetics (k_{oc}) (Eq. S183).

$$f(t_o') = N_e \cdot e^{-k_{oc} \cdot t_o'} \quad (\text{Eq. S185})$$

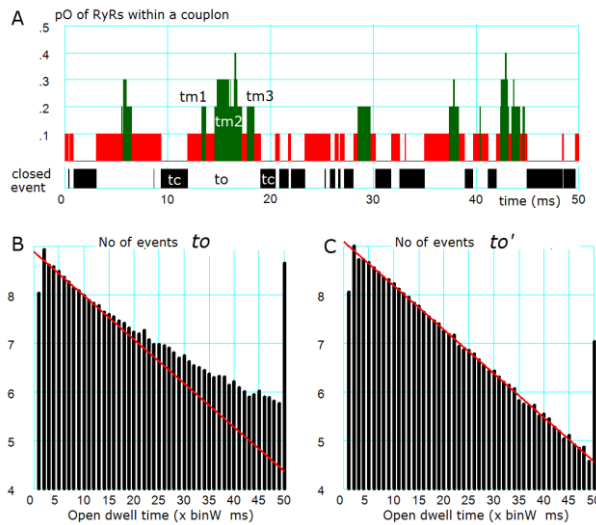


Fig. S3 Dwell time histograms for t_o and t_o' obtained from stochastic calculation of a couplon consisting of RyRs ($N_{\text{RyR}} = 10$) at $[\text{Ca}]_{\text{nd}} = 50 \mu\text{M}$. A: probability of open RyRs within a couplon. Black, red and green colours indicate durations that none, one, or multiple RyRs are open at the time. The closed, open, and multiple open time durations are indicated by t_c , t_o and $t_{m,i}$ ($i = 1 \sim k$), respectively. B; dwell time histogram for t_o , fitted with a monoexponential function with $\tau = 1/k_{oc}$. C: dwell time histogram for t_o' , fitted with the same monoexponential function as in B. The large

number of events at the last bin in the histogram are the sum of events observed at longer open dwell time than the maximum value of 50×0.1 (binwidth) = 5 ms.

Determination of closing rate of a couplon, β

According to the findings described above, the closing rate of a couplon (β) might be determined from the closing rate k_{oc} of RyR, provided that the fraction t_o' / t_o is predicted. Based on the fact that all the remaining RyRs ($N_{RyR} - 1$) are closed during t_o' except the single open RyR, this probability of simultaneous closure of ($N_{RyR} - 1$) RyRs will be approximated by $pC^{(N_{RyR}-1)l}$.

$$t_o' \approx g(t_o) = t_o \cdot pC^{(N_{RyR}-1)l} \quad \text{or} \quad \frac{t_o'}{t_o} \approx pC^{(N_{RyR}-1)l} \quad (\text{Eq. S186})$$

where pC is the steady state closed probability of a single RyR (Eq. S187), and l is a correction factor.

$$pC = \frac{k_{oc}}{k_{co} + k_{oc}} \quad (\text{Eq. S187})$$

Then, the distribution of couplon open times t_o is given by,

$$f(g(t_o)) \approx N_e \cdot e^{-k_{oc} \cdot t_o \cdot pC^{(N_{RyR}-1)l}} = N_e \cdot e^{-\beta \cdot t_o} \quad (\text{Eq. S188})$$

and

$$\beta = k_{oc} \cdot pC^{(N_{RyR}-1)l} \quad (\text{Eq. S189})$$

Lastly, we fixed the correction factor, l , by performing stochastic simulations for various $[Ca]_{nd}$. We calculated the ensemble average of $N_e = 5000$ open events as shown by an example at $50 \mu\text{M}$ $[Ca]_{nd}$ in Fig. S4A, which was well fitted with a single exponential function (red curve) using the least squares method. The closing rates of a couplon thus obtained at various $[Ca]_{nd}$ are plotted in Fig. S4B for the LC model (red). The same analysis was also applied to our couplon model in HuVEC model and results were plotted by black symbols. The two continuous curves, red and black

superimposed on the data points, were drawn by Eq. S189 using a common l fixed at 0.74. We also confirmed that Eq. S189 was applicable to couplons consisting of 1~20 RyRs.

In brief, we conclude that the closing rate defined by the two state transition model of a couplon is different from that of single RyR kinetics because of overlaps of MOEs during the ‘open time of a couplon’.

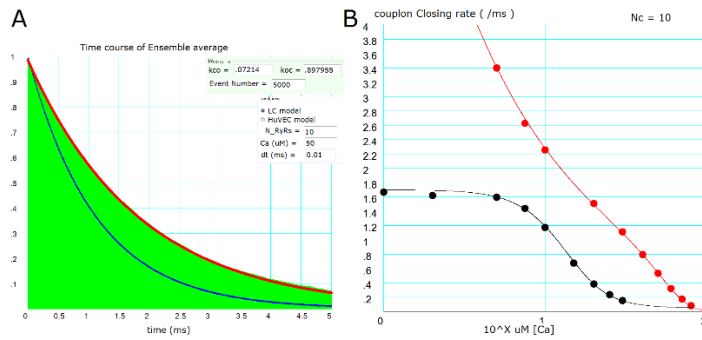


Fig. S4 Determination of the closing rate β for the two-state couplon model.

A: Ensemble mean of couplon open times. The ensemble mean of open times (t_o) was constructed by cumulating individual open events during the course of stochastic computation of 10 RyRs within a couplon until 5000 events were accumulated (Green area) by applying 50 μM $[\text{Ca}]_{\text{nd}}$ to the LC model. The red exponential curve was fitted by the least squares method. The blue exponential curve was drawn using the k_{oc} of single RyR for comparison. B: Red circles illustrate data points of β obtained by applying the least squares method to the ensemble mean at various $[\text{Ca}]_{\text{nd}}$ indicated on the abscissa of logarithmic scale. The continuous curve was drawn by the empirical formula of Eq. S189 with $l = 0.74$. Red symbols are derived from the couplon of LC model, and black symbols are from that of HuVEC model.

Comparison of activation and deactivation rates of a RyR or couplon among different models

In the SJ, LC, SM(toy) and our HuVEC models, the gating of a single RyR is described using the two-state kinetic scheme, and the rate constants are based on the single channel recordings in the planar lipid bilayer method. The activation rates are all dependent on $[\text{Ca}^{2+}]$ with a cooperativity factor (n_H) of 2 ~ 4. In our model, the activation rate of a single RyR (red line) was determined by adjusting the rate used in SM model (blue line).

Table S6 Comparisons among mathematical descriptions of the couplon activation

	Spark CICR model		Whole cell CICR model	
	SJ model	SM 'toy' model	HuVEC model	Hinch model
Activation rate	$\frac{k_o \cdot CF_{open}}{1 + (\frac{K}{Ca})^4}$	$k_o \cdot Ca^2 \cdot (sloc0 + Ca_{sr})$ $Ca = \frac{i \cdot n_{open}}{8\pi FhD} + cao$	$\overline{k_{rco}}$ (Eq. 9) $k_{rco} = (f_n \cdot k_{co}) \cdot f_i \cdot (sloc0 + Ca_{SRrl})$ $k_{co}(Ca_{LR/0R}) = \frac{1}{1 + (\frac{K}{Ca_{nd}})^{2.7}}$ $f_i = \frac{k_{co}(Ca_{L0/00})}{k_{co}(Ca_{L0/00}) + k_c}$	$\frac{k_o}{1 + (\frac{K}{Ca_{L0/00}})^2}$
Deactivation rate	$k_c \cdot CF_{close}$	k_c	$k_c \cdot pC^{(N_{Rr}^{-1})^l}$	k_c
Reference local Ca^{2+} for RyR or couplon activation	$\frac{d[Ca]_{ss}}{dt} = J_{LCC} + J_{RyR} + J_D$	$[Ca]_{dc} = f_{SMtoy}(J_{RyR})$	$[Ca]_{nd} = f_{HuVEC}(J_{LCC}, J_{RyR}, [Ca]_{jnc}, [Ca]_{SRrl}, [Ca]_o)$ (Eq. 2)	$[Ca]_{ds} = f_{Hinch}(J_{LCC}, [Ca]_i)$
next compartment	<i>blk</i>	<i>n.c</i>	<i>jnc</i>	<i>blk</i>

k_o, k_c ; opening and closing rate constants of a RyR, CF_{open} and CF_{close} ; cooperative factor for open and close rate, i ; single RyR channel current, $(sloc0 + Ca_{sr})$; the SR Ca^{2+} -content factor, pC ; probability of closed state, N_{RyR} ; number of RyRs within a couplon, l ; correcting factor, ss ; subspace, dc ; dyadic cleft, ds ; dyadic space, K ; a half saturation $[Ca^{2+}]$, J_x ; Ca^{2+} flux via X per unit volume and *n.c.*; not concerned. No empirical equations are given in LC model.

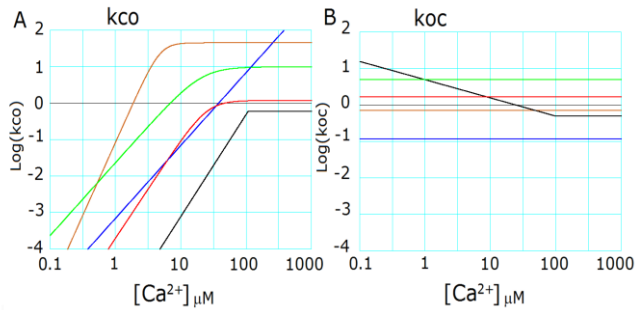


Fig. S5. Kinetics of RyRs

Relationships between $[Ca^{2+}]$ and open (Fig. S5A) and close rates (Fig. S5B), in five model studies are shown in each panel respectively. Black: LC model, Blue: SM model, Lime: Hinch model, Chocolate: SJ model, Red: HuVEC model. A $[Ca^{2+}]_{SRrl}$ of $500 \mu M$ was used to calculate rate of activation if necessary.

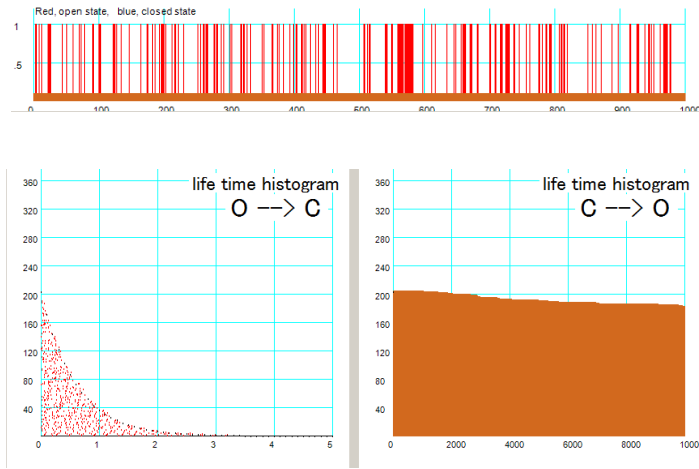


Fig. S6. Stochastic simulation of 20,000 couplons activity and its life time histogram ($Ca_{00}=0.2\mu M$, $SRCa=0.6mM$, $Ca_{0R}=0.15mM$). Top) red vertical lines show 203 open events of 20,000 couplons occurred in 1000 ms. Bottom: open and close life time histogram obtained after 20,000 sweeps of stochastic simulations including 196 open events show smoothed time courses of the activation and inactivation of couplons.

Implementation of 'blink space (*bs*)' in HuVEC model

In order to examine the involvement of 'blinks' in determining the time course of CICR extinction, we newly assume a 'blink space' (*bs*) under the junctional SR membrane supporting the couplon as schematically shown in Fig. S7. The parameters in this figure are denoted in analogy to the HuVEC (Hinch) dyadic space model.

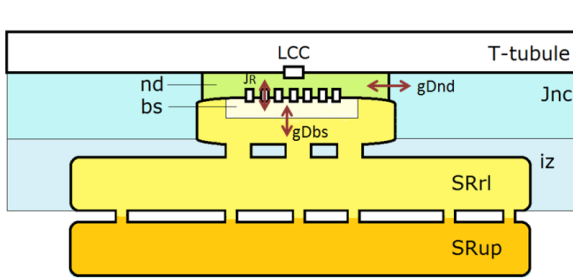


Fig. S7. Schematic representation of the dyadic model. J_R ; Ca^{2+} permeability of single couplon ($\mu m^3/ms$), g_{Dbs} ; Ca^{2+} flux rate from *SRrl* to *bs* ($\mu m^3/ms$), g_{Dnd} ; Ca^{2+} flux rate from *nd* to *jnc* ($\mu m^3/ms$), Ca_{bs} ; Ca^{2+} concentration in *bs* (mM), Ca_{SRrl} ; Ca^{2+} concentration in *SRrl* (mM).

According to the simultaneous recording of both sparks and blinks (39-41) the time course of a blink is nearly a mirror image of a spark, indicating that the depletion and the replenishment of Ca^{2+} in *bs* is quite rapid. Since each pair of spark-blink of a similar time course is evoked by the same Ca^{2+} flux via a couplon, the balance between the Vol_{bs} and g_{Dbs} should be comparable to that between Vol_{nd} and g_{Dnd} . If so, $[Ca^{2+}]_{bs}$ (Ca_{bs}) might be given as an instantaneous function of J_R and g_{Dbs} in analogy to $[Ca^{2+}]_{ds}$ in the Hinch formalism. The rate of change in Ca_{bs} is,

$$\frac{dCa_{bs}}{dt} = \frac{-J_R \cdot (Ca_{bs} - Ca_{nd}) + gD_{bs} \cdot (Ca_{SRrl} - Ca_{bs})}{Vol_{bs}} \quad (\text{Eq. S190})$$

If a rapid equilibrium of Ca^{2+} diffusion is assumed within the blink space in Eq. S190, namely, $dCa_{bs}/dt = 0$

$$J_R \cdot (Ca_{bs} - Ca_{nd}) = gD_{bs} \cdot (Ca_{SRrl} - Ca_{bs}) . \quad (\text{Eq. S191})$$

Eq. S191 is comparable to the original Hinch algorithm for the instantaneous balance of Ca^{2+} fluxes at nd .

$$J_R \cdot (Ca_{bs} - Ca_{nd}) = gD_{nd} \cdot (Ca_{nd} - Ca_{00}) \quad (\text{Eq. S192})$$

From Eqs. S191 & S192, Ca_{bs} and Ca_{nd} is given as an instantaneous function of Ca_{00} and Ca_{SRrl} . For example, when a couplon is open and LCC is closed, Ca_{bs} and Ca_{nd} are determined by Eqs. S193 & S194.

$$Ca_{bs} = \frac{\frac{Ca_{00}}{1+f_R} + \frac{Ca_{SRrl}}{f_{bs}}}{\left(1 + \frac{1}{f_{bs}} - \frac{f_R}{1+f_R}\right)} \quad (\text{Eq. S193})$$

and

$$Ca_{nd} = Ca_{0R} = \frac{Ca_{00} + f_R \cdot Ca_{bs}}{1 + f_R}, \quad (\text{Eq. S194})$$

where

$$f_R = \frac{J_R}{gD_{nd}} \quad (\text{Eq. S195})$$

and

$$f_{bs} = \frac{J_R}{gD_{bs}} . \quad (\text{Eq. S196})$$

When the couplon is closed,

$$Ca_{bs} = Ca_{SRrl} . \quad (\text{Eq. S197})$$

Namely, Ca_{bs} switches between these two concentrations according to the open-close transitions of the couplon. This instantaneous relationship of Ca_{bs} can be readily applied to the compound state transition model of CaRU (36). When $gD_{bs} = \infty$, then $Ca_{bs} = Ca_{SRrl}$ and $Ca_{nd} = Ca_{0R}$ as in the original HuVEC model, and when $gD_{bs} = 0$, then $Ca_{bs} = Ca_{nd} = Ca_{00}$.

Using the dyadic model newly developed as above, the relationship between the degree of local SR depletion and the activation and deactivation of a couplon, (k_{rco} and k_{roc}), was determined by varying the ratio of gD_{bs} and gD_{nd} ($r_{bs} = gD_{bs} / gD_{nd}$) at various levels of Ca_{SRrl} (Fig. S8).

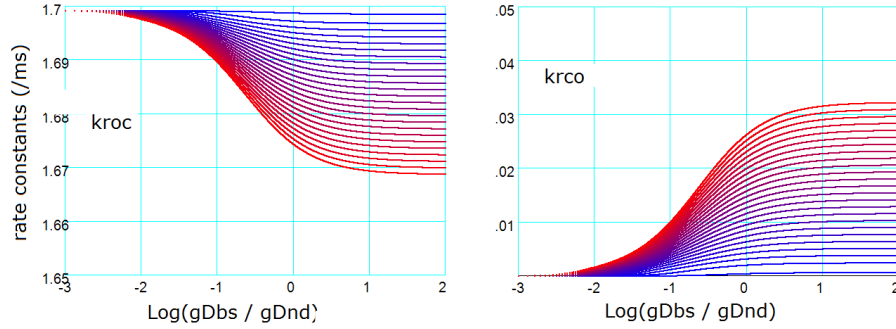


Fig. S8. Rate constants calculated using the dyadic model at various r_{bs} ($Ca_{00}=2 \mu M$, $[Ca^{2+}]_{SRrl}=0.1\sim 5 \text{ mM}$). $[Ca^{2+}]_{SRrl}$ was changed to various levels from 0.1 to 5 mM in increments of 0.2 mM. k_{roc} and k_{rco} was colored in a gradient manner according to $[Ca^{2+}]_{SRrl}$ (blue at $[Ca^{2+}]_{SRrl} = 0.1 \text{ mM}$ and red at $[Ca^{2+}]_{SRrl} = 5 \text{ mM}$).

Considering $[Ca^{2+}]_{SRrl} = \sim 0.6 \text{ mM}$ at resting condition, it may be concluded that a single couplon could exhibit a train of open events at higher $[Ca^{2+}]_{SRrl}$, which would be achieved by increasing Ca^{2+} flux rate from SRrl to bs (gD_{bs}) or SR Ca^{2+} loading by, for example, pharmacological treatment.

Frequency-dependency of HuVEC model

For validation of HuVEC model, the frequency-dependencies of $[Na^+]_{cyt}$, APD_{90} , $[Ca^{2+}]_{SRrl}$ and the peak amplitude of Ca^{2+} transient were examined (Fig. S9). At every stimulus frequency, all these measurements reached stable values, and responses were completely reversible after returning to the control frequency. The APD_{90} smoothly decreased with increasing stimulation rate as reported in both experimental and simulation studies (21, 24, 42-44). This decrease of APD_{90} was largely due to the increase in outward I_{NaK} amplitude induced by the accumulation of $[Na^+]_{cyt}$ with increasing frequency of AP generation. The decrease in $[Ca^{2+}]_{SRrl}$ at the lower stimulus frequency was due to the Ca^{2+} leak from SR via basal openings of RyRs during diastole, while the decrease with increasing frequency above 1 Hz was due to incomplete replenishment of SR with Ca^{2+} during the shortened diastolic duration. Nevertheless, the peak of $[Ca^{2+}]_{blk}$ transient was increased with increasing frequency. This is because the diastolic level of $[Ca^{2+}]_{blk}$ was elevated, for example from the control $0.064 \mu M$ to $0.16 \mu M$ at 2.5 Hz. The shortening of APD was well correlated with the increase in I_{NaK} with increasing $[Na^+]_{cyt}$. These findings are in line with the GPB and ORd models.

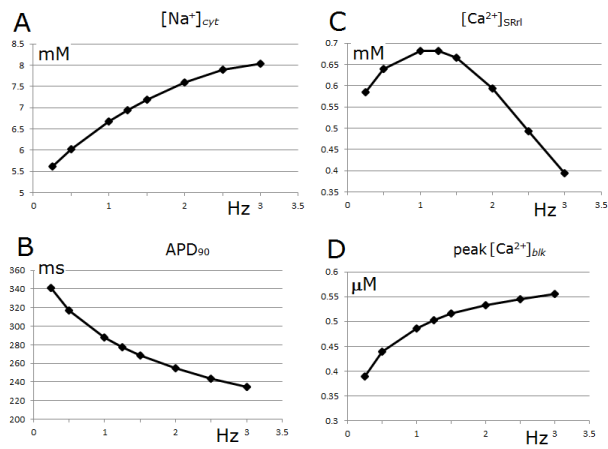


Fig. S9. Frequency-dependency of the HuVEC model

A: $[Na^+]_{cyt}$, B: APD_{90} , C: $[Ca^{2+}]_{SRrel}$, D: peak $[Ca^{2+}]_{blk}$ magnitude of isotonic F_b at 6 mN/mm^2 . The ion concentrations were measured at the end of diastole.

Initial set of time-dependent variables of HuVEC model at a standard CL of 1000 ms

Vm = -91.4466885079348
TnChCa = 0.110742559707052
CaMca = 0.000228581865602447
bufferSRCa = 0.00172960014640511
Lb_jnc = 0.0218215322629436
Lb_iz = 0.0075621764602356
Hb_jnc = 0.185094540066232
Hb_iz = 0.0769149150028914

Nai = 6.66894310282034
Ki = 139.238265011042
Catot_jnc = 0.207176351449979
Catot_iz = 0.084640522722006
Catot_blk = 0.11279654524634
Ca_SRup = 0.761077662687456
Catot_SRrl = 2.21876221622152

O_TM = 0.000000706725155695262
I2_TM = 0.0117704053067285
Is_TM = 0.304002781414015

O_LSM = 0.00000295214591324261
I1_LSM = 0.00254273877063925
I2_LSM = 0.0118261382165599
Is_LSM = 0.303220346353844

Yco_iz = 0.992251726297519
Yoc_iz = 0.000000024556270151713
Yoo_iz = 0.00000314564543512061
Yco_blk = 0.992424981547859
Yoc_blk = 0.0000000240070147854924
Yoo_blk = 0.00000314619469048683

Yooo = 0.00000172489315884865
Yooc = 0.00000142034754677507

Ycoo = 0.0000138422676498755
Ycoc = 0.992110534408681
Ycco = 0.0000000953816272498217
Yoco = 0.00000000000156949238162028
Yocc = 0.0000000249594301562175

paraxrF = 0.00000486210633393005
paraxrS = 0.437041249050081

paraxs1_iz = 0.277482694590328
paraxs2_iz = 0.000131110342877451
paraxs1_blk = 0.277482694590328
paraxs2_blk = 0.000131110342877451

a_IKto = 0.000793627635934239
y1_IKto = 0.999756080468878
y2_IKto = 0.575995954010486

Pbspm = 0.594875991179992

E1NCX_iz = 0.238718640001014
I1NCX_iz = 0.13771129457898
I2NCX_iz = 0.622892868847556
E1NCX_blk = 0.111872123711613
I1NCX_blk = 0.203023555446362
I2NCX_blk = 0.684869019924837

P1_6_NaK = 0.435289193632868
P7_NaK = 0.0831770174499825
P8_13_NaK = 0.281082409575779

halfSL = 1.09840500012898
Fb = 0.0502092089156129
Fp = 4.94926096641491
TSCa3 = 0.00899891910620064
TSCa3W = 0.000369547640656701
TSCa3S = 0.000153834503967436
TSS = 0.000876347322180234
TSW = 0.000492054058977473
hw = 0.000100147615113241
hp = 0.00600014761511324

ATPt_cyt = 6.67701543987464

ADPt_cyt = 0.0227671477707

Pi_cyt = 0.381130087573153

PCr_cyt = 13.9261301893242

Supporting References

1. Beuckelmann, D. J., M. Nabauer, and E. Erdmann. 1992. Intracellular calcium handling in isolated ventricular myocytes from patients with terminal heart failure. *Circulation* 85:1046-1055.
2. Powell, T., M. F. Sturridge, S. K. Suvarna, D. A. Terrar, and V. W. Twist. 1981. Intact individual heart cells isolated from human ventricular tissue. *British medical journal* 283:1013-1015.
3. Satoh, H., L. M. Delbridge, L. A. Blatter, and D. M. Bers. 1996. Surface:volume relationship in cardiac myocytes studied with confocal microscopy and membrane capacitance measurements: species-dependence and developmental effects. *Biophysical journal* 70:1494-1504.
4. Jost, N., L. Virag, M. Bitay, J. Takacs, C. Lengyel, P. Biliczki, Z. Nagy, G. Bogats, D. A. Lathrop, J. G. Papp, and A. Varro. 2005. Restricting excessive cardiac action potential and QT prolongation: a vital role for IKs in human ventricular muscle. *Circulation* 112:1392-1399.
5. Sakakibara, Y., T. Furukawa, D. H. Singer, H. Jia, C. L. Backer, C. E. Arentzen, and J. A. Wasserstrom. 1993. Sodium current in isolated human ventricular myocytes. *The American journal of physiology* 265:H1301-1309.
6. Mewes, T., and U. Ravens. 1994. L-type calcium currents of human myocytes from ventricle of non-failing and failing hearts and from atrium. *Journal of molecular and cellular cardiology* 26:1307-1320.
7. Li, G. R., J. Feng, L. Yue, M. Carrier, and S. Nattel. 1996. Evidence for two components of delayed rectifier K⁺ current in human ventricular myocytes. *Circulation research* 78:689-696.
8. Jost, N., L. Virag, M. Opincariu, J. Szecsi, A. Varro, and J. G. Papp. 1998. Delayed rectifier potassium current in undiseased human ventricular myocytes. *Cardiovascular research* 40:508-515.
9. Gerdes, A. M., S. E. Kellerman, J. A. Moore, K. E. Muffly, L. C. Clark, P. Y. Reaves, K. B. Malec, P. P. McKeown, and D. D. Schocken. 1992. Structural remodeling of cardiac myocytes in patients with ischemic cardiomyopathy. *Circulation* 86:426-430.
10. Laver, D. R., C. H. Kong, M. S. Imtiaz, and M. B. Cannell. 2013. Termination of calcium-induced calcium release by induction decay: an emergent property of stochastic channel gating and molecular scale architecture. *Journal of molecular and cellular cardiology* 54:98-100.
11. Sobie, E. A., K. W. Dilly, J. dos Santos Cruz, W. J. Lederer, and M. S. Jafri. 2002. Termination of

- cardiac Ca(2+) sparks: an investigative mathematical model of calcium-induced calcium release. *Biophysical journal* 83:59-78.
12. Shannon, T. R., F. Wang, J. Puglisi, C. Weber, and D. M. Bers. 2004. A mathematical treatment of integrated Ca dynamics within the ventricular myocyte. *Biophysical journal* 87:3351-3371.
 13. Asakura, K., C. Cha, H. Yamaoka, Y. Horikawa, H. Memida, T. Powell, A. Amano, and A. Noma. 2014. EAD and DAD mechanisms analyzed by developing a new human ventricular cell model. *Progress in biophysics and molecular biology*.
 14. Negroni, J. A., and E. C. Lascano. 2008. Simulation of steady state and transient cardiac muscle response experiments with a Huxley-based contraction model. *Journal of molecular and cellular cardiology* 45:300-312.
 15. Yue, D. T., and E. Marban. 1990. Permeation in the dihydropyridine-sensitive calcium channel. Multi-ion occupancy but no anomalous mole-fraction effect between Ba²⁺ and Ca²⁺. *The Journal of general physiology* 95:911-939.
 16. Peterson, B. Z., J. S. Lee, J. G. Mulle, Y. Wang, M. de Leon, and D. T. Yue. 2000. Critical determinants of Ca(2+)-dependent inactivation within an EF-hand motif of L-type Ca(2+) channels. *Biophysical journal* 78:1906-1920.
 17. Shirokov, R., R. Levis, N. Shirokova, and E. Rios. 1993. Ca(2+)-dependent inactivation of cardiac L-type Ca²⁺ channels does not affect their voltage sensor. *The Journal of general physiology* 102:1005-1030.
 18. Ferreira, G., J. Yi, E. Rios, and R. Shirokov. 1997. Ion-dependent inactivation of barium current through L-type calcium channels. *The Journal of general physiology* 109:449-461.
 19. Pelzmann, B., P. Schaffer, E. Bernhart, P. Lang, H. Machler, B. Rigler, and B. Koidl. 1998. L-type calcium current in human ventricular myocytes at a physiological temperature from children with tetralogy of Fallot. *Cardiovascular research* 38:424-432.
 20. Magyar, J., N. Iost, A. Kortvely, T. Banyasz, L. Virag, P. Sziglieti, A. Varro, M. Opincariu, J. Szecsi, J. G. Papp, and P. P. Nanasi. 2000. Effects of endothelin-1 on calcium and potassium currents in undiseased human ventricular myocytes. *Pflugers Archiv : European journal of physiology* 441:144-149.
 21. Li, G. R., J. Feng, L. Yue, and M. Carrier. 1998. Transmural heterogeneity of action potentials and Ito1 in myocytes isolated from the human right ventricle. *The American journal of physiology* 275:H369-377.
 22. Fulop, L., T. Banyasz, J. Magyar, N. Szentandrassy, A. Varro, and P. P. Nanasi. 2004. Reopening of L-type calcium channels in human ventricular myocytes during applied epicardial action potentials. *Acta physiologica Scandinavica* 180:39-47.
 23. Brunet, S., T. Scheuer, and W. A. Catterall. 2009. Cooperative regulation of Ca(v)1.2 channels by intracellular Mg(2+), the proximal C-terminal EF-hand, and the distal C-terminal domain. *The*

- Journal of general physiology 134:81-94.
24. Grandi, E., F. S. Pasqualini, and D. M. Bers. 2010. A novel computational model of the human ventricular action potential and Ca transient. *Journal of molecular and cellular cardiology* 48:112-121.
 25. Sun, L., J. S. Fan, J. W. Clark, and P. T. Palade. 2000. A model of the L-type Ca²⁺ channel in rat ventricular myocytes: ion selectivity and inactivation mechanisms. *The Journal of physiology* 529 Pt 1:139-158.
 26. Zhang, J. F., P. T. Ellinor, R. W. Aldrich, and R. W. Tsien. 1994. Molecular determinants of voltage-dependent inactivation in calcium channels. *Nature* 372:97-100.
 27. Matsuda, H. 1986. Sodium conductance in calcium channels of guinea-pig ventricular cells induced by removal of external calcium ions. *Pflugers Archiv : European journal of physiology* 407:465-475.
 28. Yan, D. H., and K. Ishihara. 2005. Two Kir2.1 channel populations with different sensitivities to Mg(2+) and polyamine block: a model for the cardiac strong inward rectifier K(+) channel. *The Journal of physiology* 563:725-744.
 29. Ishihara, K., and D. H. Yan. 2007. Low-affinity spermine block mediating outward currents through Kir2.1 and Kir2.2 inward rectifier potassium channels. *The Journal of physiology* 583:891-908.
 30. Jost, N., L. Virag, P. Comtois, B. Ordog, V. Szuts, G. Seprenyi, M. Bitay, Z. Kohajda, I. Koncz, N. Nagy, T. Szel, J. Magyar, M. Kovacs, L. G. Puskas, C. Lengyel, E. Wettwer, U. Ravens, P. P. Nanasi, J. G. Papp, A. Varro, and S. Nattel. 2013. Ionic mechanisms limiting cardiac repolarization reserve in humans compared to dogs. *The Journal of physiology* 591:4189-4206.
 31. Rajamani, S., L. L. Eckhardt, C. R. Valdivia, C. A. Klemens, B. M. Gillman, C. L. Anderson, K. M. Holzem, B. P. Delisle, B. D. Anson, J. C. Makielski, and C. T. January. 2006. Drug-induced long QT syndrome: hERG K⁺ channel block and disruption of protein trafficking by fluoxetine and norfluoxetine. *British journal of pharmacology* 149:481-489.
 32. Takeuchi, A., S. Tatsumi, N. Sarai, K. Terashima, S. Matsuoka, and A. Noma. 2006. Ionic mechanisms of cardiac cell swelling induced by blocking Na⁺/K⁺ pump as revealed by experiments and simulation. *The Journal of general physiology* 128:495-507.
 33. Oka, C., C. Y. Cha, and A. Noma. 2010. Characterization of the cardiac Na⁺/K⁺ pump by development of a comprehensive and mechanistic model. *Journal of theoretical biology* 265:68-77.
 34. Smith, N. P., and E. J. Crampin. 2004. Development of models of active ion transport for whole-cell modelling: cardiac sodium-potassium pump as a case study. *Progress in biophysics and molecular biology* 85:387-405.
 35. Grandi, E., F. S. Pasqualini, C. Pes, C. Corsi, A. Zaza, and S. Severi. 2009. Theoretical

- investigation of action potential duration dependence on extracellular Ca^{2+} in human cardiomyocytes. *Journal of molecular and cellular cardiology* 46:332-342.
36. Hinch, R., J. L. Greenstein, A. J. Tanskanen, L. Xu, and R. L. Winslow. 2004. A simplified local control model of calcium-induced calcium release in cardiac ventricular myocytes. *Biophysical journal* 87:3723-3736.
 37. Tran, K., N. P. Smith, D. S. Loiselle, and E. J. Crampin. 2009. A thermodynamic model of the cardiac sarcoplasmic/endoplasmic Ca^{2+} (SERCA) pump. *Biophysical journal* 96:2029-2042.
 38. Negroni, J. A., and E. C. Lascano. 1996. A cardiac muscle model relating sarcomere dynamics to calcium kinetics. *Journal of molecular and cellular cardiology* 28:915-929.
 39. Brochet, D. X., D. Yang, A. Di Maio, W. J. Lederer, C. Franzini-Armstrong, and H. Cheng. 2005. Ca^{2+} blinks: rapid nanoscopic store calcium signaling. *Proceedings of the National Academy of Sciences of the United States of America* 102:3099-3104.
 40. Zima, A. V., E. Picht, D. M. Bers, and L. A. Blatter. 2008. Termination of cardiac Ca^{2+} sparks: role of intra-SR $[\text{Ca}^{2+}]$, release flux, and intra-SR Ca^{2+} diffusion. *Circulation research* 103:e105-115.
 41. Brochet, D. X., W. Xie, D. Yang, H. Cheng, and W. J. Lederer. 2011. Quarky calcium release in the heart. *Circulation research* 108:210-218.
 42. Li, G. R., B. Yang, J. Feng, R. F. Bosch, M. Carrier, and S. Nattel. 1999. Transmembrane I_{Ca} contributes to rate-dependent changes of action potentials in human ventricular myocytes. *The American journal of physiology* 276:H98-H106.
 43. Pieske, B., B. Kretschmann, M. Meyer, C. Holubarsch, J. Weirich, H. Posival, K. Minami, H. Just, and G. Hasenfuss. 1995. Alterations in intracellular calcium handling associated with the inverse force-frequency relation in human dilated cardiomyopathy. *Circulation* 92:1169-1178.
 44. O'Hara, T., L. Virag, A. Varro, and Y. Rudy. 2011. Simulation of the undiseased human cardiac ventricular action potential: model formulation and experimental validation. *PLoS computational biology* 7:e1002061.